

# Anisotropic Viscoelasticity and Wrinkling of Super-Pressure Balloons: Simulation and Experimental Verification

T. Gerngross\*

*University of Cambridge, Cambridge, UK*

S. Pellegrino†

*California Institute of Technology, Pasadena, CA*

Super-pressure balloons are currently under development by the NASA Balloon Program Office for use in stratospheric balloon missions. They are made of thin polyethylene film forming a sealed envelope that is contained by stiff meridional tendons. The film is subject to a state of stress whose details depend on the cutting pattern, stiffness of the film vs. stiffness of the tendons, etc. and the viscoelastic behavior in the film plays an important role. This paper extends the modeling approach presented by the same authors at the AIAA Balloon Systems Conference 2007. The current model captures nonlinear viscoelasticity in a wrinkled, anisotropic membrane, and the analysis has been successfully applied to several balloon designs. Because the effects of wrinkling on the stress history are modeled correctly, the behavior of the balloon can be simulated with high fidelity, starting from pressures as low as 5-20 Pa. The creep strains at selected points of a 4 m diameter balloon were measured using photogrammetry and the results were compared to results from the numerical model. At a pressure of 700 Pa the balloon had a maximum stress of 6.0 MPa in the meridional direction (2.5 MPa hoop stress) and meridional strains of up to 6.4% (-2.7% hoop strain). A detailed model of gore seams and tendon attachments provides insight into the asymmetry of the strain distribution that results from the actual asymmetry of the gore seams. This also allows the numerical replication of an experimentally observed pressure-dependent rotation of the end-fittings.

## I. Introduction

Super-pressure balloons are currently under development by the NASA Balloon Program Office for use in stratospheric balloon missions. They are made of thin polyethylene film forming a sealed envelope that is contained by a series of meridional tendons. The film is subject to a state of stress whose details depend on the cutting pattern, stiffness of the film vs. stiffness of the tendons, etc. Viscoelastic effects, which are significant in the film, play an important role in the stress distribution and shape of these balloons. Experiments on small scale ground models have shown that wrinkles are present over a wide range of pressures. With increasing pressures and/or after some time under pressurization these wrinkles eventually disappear.

The complex behaviour of these balloons is being studied in more and more detail and numerical models of increasing sophistication are currently under development and are also being validated experimentally. This in turn requires that both time-dependent material behavior and wrinkling behavior be included in the models. An algorithm has been developed for anisotropic material behavior that implements a biaxial viscoelastic model recently derived by Rand<sup>11,12</sup> and also allows wrinkling effects to be considered. This algorithm has been implemented as a user-defined material (UMAT) in Abaqus.

---

\*Graduate Student, Department of Engineering, Trumpington Street, CB2 1PZ. [tg247@cam.ac.uk](mailto:tg247@cam.ac.uk)

†Professor of Aeronautics and Civil Engineering, Graduate Aerospace Laboratories, 1200 E. California Blvd. MC 301-46. AIAA Fellow. [sergiop@caltech.edu](mailto:sergiop@caltech.edu)

In this paper the modeling approach that was presented by Gerngross and Pellegrino<sup>5</sup> at the AIAA Balloon Systems Conference 2007 has been further developed. The current model is capable of modeling nonlinear viscoelasticity in a wrinkled, anisotropic membrane, and the analysis has been successfully applied to several balloon designs. Because the effects of wrinkling on the stress history are modeled correctly, the behavior of the balloon can be simulated with high fidelity, starting from pressures as low as 5-20 Pa. In order to demonstrate the accuracy of the implemented algorithm, the creep strains at selected points of a 4 m diameter balloon were measured using photogrammetry. High accuracy creep measurements at different pressure levels were carried out on a balloon manufactured by Aerostar. The experimental results are then compared to results from the numerical model. Lastly a more detailed model of the physical configuration of gore seams and tendon attachments is created and its results provide insight into the asymmetry of the strain distribution that results from the actual asymmetry of the gore seams. This also allows the numerical replication of an experimentally observed swirl in the end-fitting region.

## II. Background

### II.A. Material

The polyethylene film that is currently used for NASA Super-Pressure Balloons is called StratoFilm 420. It is produced as a three layer co-extrusion of a Linear Low Density Polyethylene (LLDPE) called Dowlex 2056G. The three layers have the thickness proportions 20/60/20 with the outer layers containing an ultra violet inhibitor (UVI) to protect the inner layer from radiation damage.<sup>11,12</sup> The nominal film thickness is 38 micron and measurements after production by L. Young have shown a range between 32.5 - 39.8 micron. In a typical extrusion process a tube of polyethylene is being pulled out of a die (the direction of pulling is called the machine direction MD) and simultaneously stretched in the transverse direction (TD). A measure of how much a film is stretched in the transverse direction is the bubble-to-die diameter called blow-up-ratio (BUR). StratoFilm SF420 has a BUR of 2 to achieve a nearly balanced film with similar properties in MD and TD.<sup>14</sup> However, the extrusion process still results in somewhat orthotropic material properties. The material properties of StratoFilm SF420 are described in the following by a nonlinear viscoelastic material model.

The small scale balloon model used for the experimental verification presented in Section IV was made of SF430 film, the same material as SF420 but without the UV-filter additive in the outer layers.

### II.B. Viscoelastic Model

#### II.B.1. Creep Law

A general introduction to the field of nonlinear viscoelasticity is provided in textbooks.<sup>8,18</sup> In reference 3 we have presented an attempt to model the time-dependent material behavior of LLDPE using the creep/relaxation models available in the implicit finite-element software Abaqus/Standard. Additionally the Schapery<sup>15</sup> nonlinear viscoelastic constitutive material model has been implemented as a user defined material (UMAT) for use in Abaqus/Standard and verified by means of cylindrical balloon structures.<sup>3,4</sup> This alternative approach is quite accurate and will be used in the following sections.

Schapery's material model<sup>15</sup> is based on the thermodynamics of irreversible processes, where the transient material behavior is defined by a master creep function. Nonlinearities can be considered by including factors that are functions of stress and temperature. Further, horizontal shift factors enable coverage of wide temperature/stress ranges. Schapery also gave a general multiaxial formulation with the nonlinear function being an arbitrary function of stress. Since the Poisson's ratio has only a weak time-dependence a single time-dependent function is sufficient to characterize all elements of the linear viscoelastic creep compliance matrix.<sup>16</sup>

Rand and co-workers<sup>13,14</sup> further simplified this relationship by assuming that the time-dependence in any material direction is linearly related to that observed in the machine direction:

$$\varepsilon_i^t = g_0^t S_{ij}^0 D_0 \sigma_j^t + g_1^t \int_0^t S_{ij} \Delta D^{(\psi^t - \psi^\tau)} \frac{d(g_2^\tau \sigma_j^\tau)}{d\tau} d\tau \quad (1)$$

where  $i, j = 1, 2$  correspond to normal strain/stress components in the machine and transverse directions of the film, respectively, and  $i, j = 6$  corresponds to the engineering shear strain/stress. Also, the reduced time

is

$$\psi^t = \int_0^t \frac{d\tau}{a_\sigma(T, \sigma) a_T(T)} \quad (2)$$

The first term in Equation (1) represents the elastic response of the material, provided by the instantaneous elastic compliance  $D_0$ , while the second term describes the transient response, defined by the transient compliance function,  $\Delta D$ . The other parameters are nonlinearity functions and horizontal shift factors for the master curve.  $S_{ij}^0$  and  $S_{ij}$  are coefficient matrices enabling the multiaxial formulation. Since the material response in any direction is based on the properties in the machine direction, one assumes  $S_{11}^0 = 1$  and  $S_{11} = 1$ . Anisotropic behavior is accounted for by adjusting the remaining coefficients.

### II.B.2. Material Parameters

The transient compliance  $\Delta D$  is given at a reference temperature of 293.16 K, assuming an instantaneous compliance  $D_0 = 3e^{-4}$  [1/MPa], Figure 1. It can be described by a sum of exponentials called a Prony Series  $\sum D_i \left[1 - \exp\left(-\frac{t}{\tau_i}\right)\right]$  with the components  $D_i$  [1/MPa] and  $\tau_i$  [s] as in Table 1.

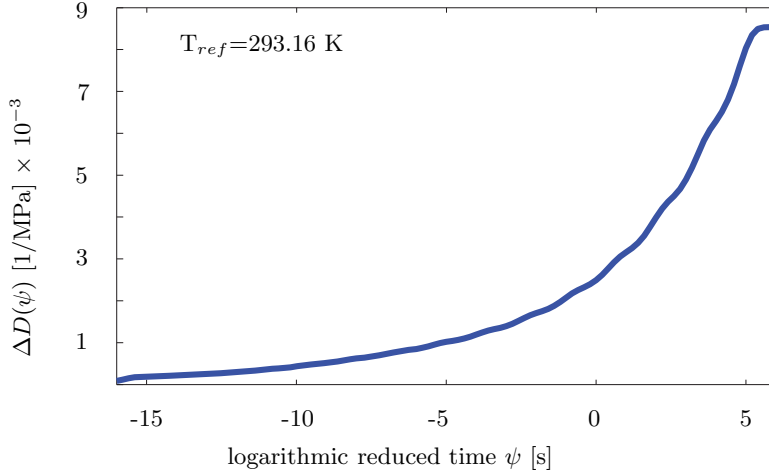


Figure 1: Transient creep compliance  $\Delta D(\psi)$

i	$D_i$ [1/MPa]	$\tau_i$ [s]
1	1.8764e-4	1.6548e-16
2	2.9249e-5	4.8697e-15
3	5.8224e-5	1.4330e-13
4	8.7542e-5	4.2170e-12
5	1.1561e-4	1.2409e-10
6	1.4159e-4	3.6517e-9
7	1.6989e-4	1.0746e-7
8	2.0924e-4	3.1623e-6
9	2.7274e-4	9.3057e-5
10	3.7796e-4	2.7384e-3
11	5.4670e-4	8.0582e-2
12	8.0581e-4	2.3714
13	1.1844e-3	69.783
14	1.7204e-3	2053.5
15	2.6285e-3	60430

Table 1: Prony series for SF420<sup>11</sup>

The temperature shift factor  $a_T$  was originally obtained for both machine and transverse direction. However, the temperature dependence in transverse direction was found to be virtually identical to that in the machine direction and hence both directions can be described by:

$$\begin{aligned} \log a_T &= (T - 293.16)[7.33e^{-4}(T - 273.16) - 0.179133] & T > 233.16 \\ \log a_T &= 3.1068 - 0.2350275(T - 273.16) & T < 233.16 \end{aligned} \quad (3)$$

The coefficients  $S_{ij}$  for the biaxial model are based on the master curve in the machine direction, hence  $S_{11}=1$ . The ratio between machine and transverse compliance results in the following temperature dependent  $S_{22}$

$$S_{22} = 1.122 + 6.5895e^{-4} T - 6.609e^{-6} T^2 \quad (4)$$

The remaining biaxial coefficients were determined to be constants:

$S_{12} = S_{21}$	$S_{66}$
-0.58	4.45

Since the instantaneous portion of the strain is very small at any stress level, Rand argued that the nonlinearity of the elastic response is negligible, hence  $g_0$  was set to unity. The remaining parameters,  $g_1$  and  $g_2$ , control the non-linearity in the transient portion of the strain, however only one parameter can be determined uniquely from the experimental data and hence only  $g_2$  was used and  $g_1$  was set to unity. The parameters  $g_2$  and  $a_\sigma$  were defined as follows

$$g_2 = 1 + 0.1875 (\sigma_{eff} - \sigma_0) \quad (5)$$

$$\log a_\sigma = -0.126 (\sigma_{eff} - \sigma_0) \quad (6)$$

where the temperature dependent  $\sigma_0$  (in MPa) determines the onset of nonlinearity:

$$\sigma_0 = 69.527 - 0.430944 T + 6.7962e^{-4} T^2 \quad (7)$$

The effective stress  $\sigma_{eff}$  allows the nonlinear effects to remain scalar functions of a single stress:

$$\sigma_{eff} = \sqrt{\sigma_1^2 + 2A_{12}\sigma_1\sigma_2 + A_{22}\sigma_2^2 + A_{66}\sigma_{12}^2} \quad (8)$$

The constant coefficients  $A_{ij}$  that allow for different influence of individual stress components on the effective stress were defined as follows:

$A_{12}$	$A_{22}$	$A_{66}$
-0.4	1.44	0.8

### II.C. Wrinkling Model

Thin membranes cannot carry compressive stresses and consequently wrinkles or slack regions will form. Most balloon structures develop wrinkles, at least during pressurization and especially near any end fittings and tendons. Experimental observations have shown that wrinkles appear even in a flat facet balloon structure.<sup>1</sup> In order to allow for experimental validation of numerical models it is important to consider the effects of wrinkling in thin anisotropic film.

In the following we present a method to predict the correct stresses and displacements in a partially wrinkled anisotropic membrane. Our aim is not to model the exact shape of the wrinkles but rather the average surface. Also the following is limited to flat membranes with in-plane loading. For a wrinkled state we make the following assumptions: the bending stresses in the membrane are negligible, the stress across a wrinkle is zero and there is a uniaxial stress along the wrinkle. A solution is obtained in four steps, as follows, for each integration point of every element:

- Step 1 Decide if the element is wrinkled (at this particular point) using an appropriate wrinkling criterion;
- Step 2 If it is wrinkled determine the wrinkle direction;
- Step 3 Compute the state of stress carrying out a correction that removes any compressive stresses;
- Step 4 Update the elasticity matrix considering that stresses cannot be carried across wrinkles.

More details are provided next.

**Step 1:** A combined stress-strain criterion based on principal strains and estimated principal stresses, denoted by the superscript  $p$ , was found to be best to determine if an element is wrinkled or not. Three different states are considered:

$$\begin{array}{ll} \text{principal stress } \sigma_{22}^p > 0 & \text{taut} \\ \text{principal strain } \varepsilon_{11}^p \leq 0 & \text{slack} \\ \text{otherwise } (\sigma_{22}^p \leq 0 \text{ and } \varepsilon_{11}^p > 0) & \text{wrinkled} \end{array}$$

**Step 2:** Kang and Im<sup>7</sup> have presented a scheme where the orientation and the magnitude of the uniaxial tension is obtained from an invariant relationship between the normal strain component in the direction of the local uniaxial tension and the engineering shear strain. They showed that for a membrane subject to a uniaxial state of stress, denoted by the superscript  $u$ , in the direction  $x$  the following two relationships are satisfied

$$\gamma_{xy}^y = \frac{C_{22}C_{61} - C_{21}C_{62}}{C_{26}C_{62} - C_{22}C_{66}} \cdot \varepsilon_x^y \quad (9)$$

$$\varepsilon_y^y = \frac{C_{12}C_{66} - C_{26}C_{61}}{C_{26}C_{62} - C_{22}C_{66}} \cdot \varepsilon_x^y \quad (10)$$

$C_{ij}$  are the components of the stress-strain relations in a coordinate system  $x, y$  where  $x$  is parallel to the direction of the wrinkles and  $y$  is orthogonal to  $x$ . The convention for  $i, j$  was explained in Section II.B.1.

Kang and Im found that Equation 9 is invariant with respect to the amplitude of the wrinkles and is also valid for both wrinkled states and (unwrinkled) uniaxial tension. Equation 10 holds only for a natural uniaxial stress, without wrinkling.

**Step 3:** Once the wrinkling direction is known, the stress across the wrinkles is set to zero.

**Step 4:** A modified elasticity matrix is created following an approach analogous to the variable Poisson's ratio approach by Miller and Hedgepeth.<sup>9,10</sup> The stress-strain relations are modified by setting the stiffness in the wrinkling direction equal to zero and compressive stresses are thus eliminated.

### III. Modeling Time-dependent Material Behavior in a Wrinkled Element

#### III.A. Abaqus Interface

In a nonlinear analysis the solution is found by specifying the loading as a function of time and incrementing time to follow the nonlinear response. Therefore, Abaqus breaks the simulation into a number of time increments and finds the approximate equilibrium configuration at the end of each time increment. Using the Newton method, it often takes Abaqus several iterations to determine an acceptable solution to each time increment.

At the beginning of each time increment the Abaqus interface for the UMAT subroutine passes the current time increment  $\Delta t$  and the corresponding strain increment  $\Delta \varepsilon_i$ . The strain increment has been determined by Abaqus based on the tangent stiffness matrix at the end of the previous time increment. Provided the material orientation has been set in the model definition, the strain components are in the local orientation.

At the end of the current time increment Abaqus requires an update of the stresses  $\sigma_j^t$  and the Jacobian matrix. For the first increment of the analysis Abaqus passes to the UMAT subroutine only a zero strain increment, in which case only the Jacobian is required. Since the strain components were provided in the local coordinate system and the stress components are also returned in the local system the Jacobian is defined as the local tangent stiffness matrix  $\partial \sigma_j^t / \partial \varepsilon_i^t$ .

In addition Abaqus provides to the UMAT subroutine an array for solution-dependent state variables. These are passed at the beginning of the increment and need to be returned with updated values at the end. This array is used to store the stress component history and the corresponding reduced time, as will be seen below.

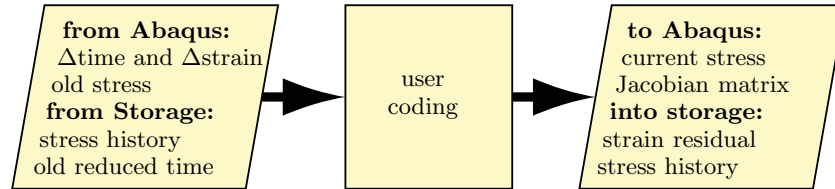


Figure 2: Abaqus interface for user-defined material behavior

#### III.B. Algorithm

Figure 3 shows the algorithm implemented in the UMAT subroutine for time-dependent anisotropic material behavior in a membrane that may also be wrinkled. This algorithm has been implemented in Abaqus, but would be equally suitable for any displacement based finite element software, where strain components are used as the independent state variables.<sup>2,5</sup>

Every time UMAT is called, it starts with an estimation of the biaxial trial stresses  $\sigma_j^{t,trial}$  based on the nonlinearity parameters at the end of the previous time increment. The principal strains and estimated principal stresses are used with a combined stress-strain criterion (Section II.C) to determine if the element is wrinkled or not. If the element is found to be taut the biaxial stresses are found in a single iteration, Subsection III.C. If the element is wrinkled, Subsection III.D describes the procedure. If the element is slack all stresses are set to zero and a zero elasticity matrix is returned, Section III.E.

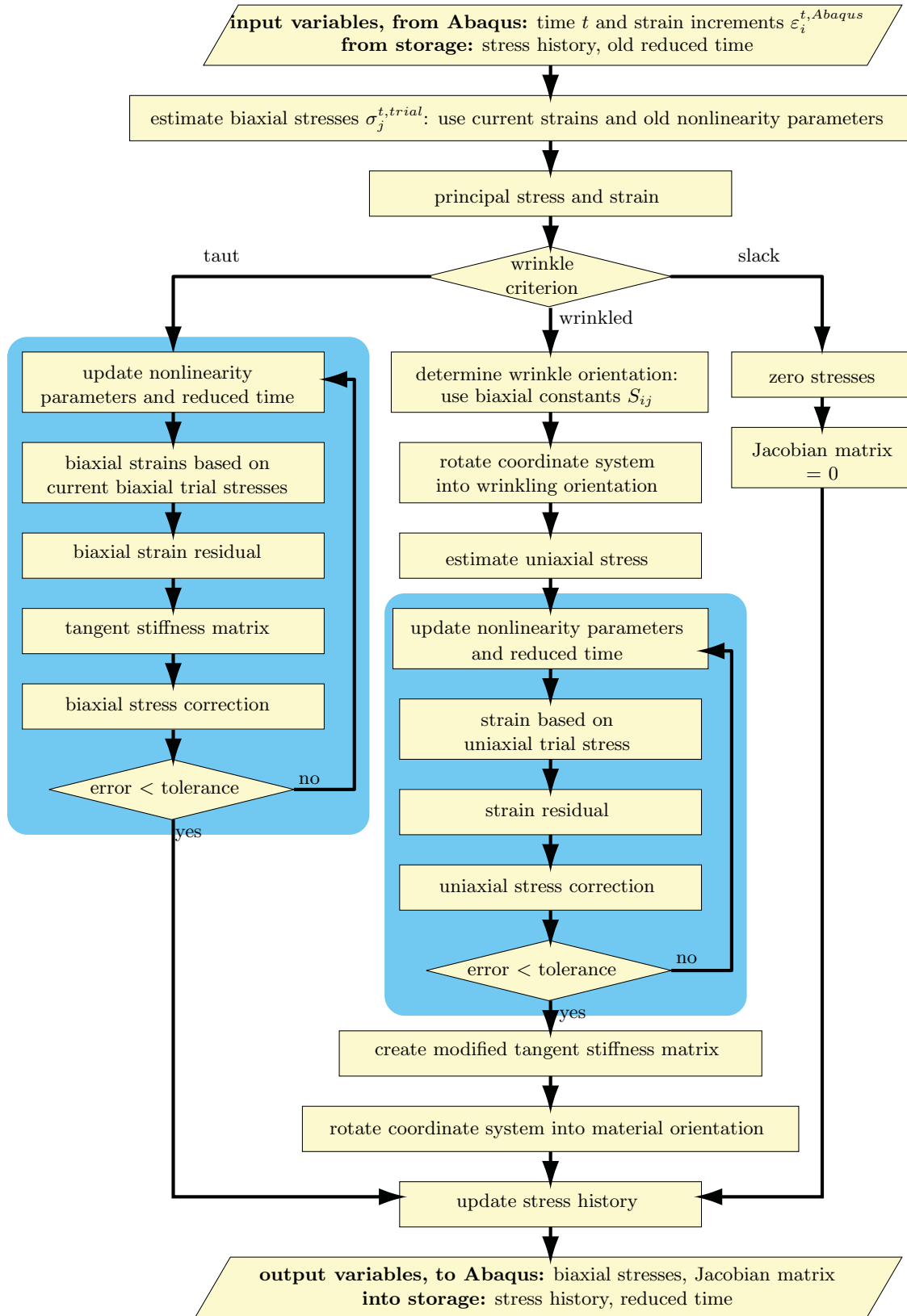


Figure 3: Algorithm for wrinkling in nonlinear viscoelastic membranes

Once the correct stresses are determined, the stress history is updated and the stresses at the end of the current time increment and the Jacobian matrix are returned to Abaqus. The stress history and the current reduced time increment are written into memory.

### III.C. Taut Membrane

If the membrane element is found to be taut, the biaxial stresses at the end of the current time increment are found by integration. A numerical integration method was presented by Haj-Ali and Muliana<sup>6</sup> for a three-dimensional, isotropic material. Based on the integration method proposed in this reference, an iterative algorithm has been developed for anisotropic material behavior that implements the biaxial model of Rand and co-workers.<sup>13,14</sup> A schematic overview of the iterative algorithm is depicted in the left column of Figure 3.

With the initial stress guess that had been used to test for wrinkling an iterative loop is entered to determine the stresses  $\sigma_j^t$  at the end of the time increment. This requires the iterative evaluation of Schapery's constitutive model, Equation 1, rewritten in incremental form as follows:

$$\begin{aligned} \varepsilon_i^t = & \left\{ g_0^t S_{ij}^0 D_0 + g_1^t g_2^t S_{ij} \sum_{n=1}^N D_n \left[ 1 - \frac{1 - \exp(-\lambda_n \Delta \psi^t)}{\lambda_n \Delta \psi^t} \right] \right\} \sigma_j^t \\ & - g_1^t S_{ij} \sum_{n=1}^N D_n \left[ \exp(-\lambda_n \Delta \psi^t) q_{j,n}^{t-\Delta t} - g_2^{t-\Delta t} \frac{1 - \exp(-\lambda_n \Delta \psi^t)}{\lambda_n \Delta \psi^t} \sigma_j^{t-\Delta t} \right] \end{aligned} \quad (11)$$

Here the heredity integrals  $q_{j,n}^{t-\Delta t}$  are computed at the end of the previous time increment. The full set of equations has been presented in reference 4 and 2. During this iteration, the strains  $\varepsilon_i^t$  due to the current trial stresses  $\sigma_j^t$  are compared to the strains  $\varepsilon_i^{t, Abaqus}$  computed by Abaqus before calling the UMAT.

If required, the stresses and the nonlinearity parameters are corrected and the loop is repeated. Alternatively, if the strain error residual is below a specified tolerance (set to  $tol = 10^{-7}$ ) UMAT exits the loop. Finally, the stress history for each of the  $n$  Prony terms and  $j$  stress components needs to be updated at the end of each time increment using

$$q_{j,n}^t = \exp(-\lambda_n \Delta \psi^t) q_{j,n}^{t-\Delta t} + \frac{1 - \exp(-\lambda_n \Delta \psi^t)}{\lambda_n \Delta \psi^t} (g_2^t \sigma_j^t - g_2^{t-\Delta t} \sigma_j^{t-\Delta t}) \quad (12)$$

### III.D. Wrinkled Membrane

If the membrane element is found to be wrinkled, the algorithm follows the center column in Figure 3. First the direction of the wrinkles in an orthotropic material needs to be found, Subsection III.D.1. Then the coordinate system is rotated to align it with the wrinkles and the correct uniaxial stress state is found with an iteration similar to that in Section III.C. Next, a modified effective elasticity matrix is computed that describes the corrected, uniaxial state of stress and keeps the stress across the wrinkles independent of any strain changes, Subsection III.D.3. Finally, the coordinate system is rotated back to the material orientation and the stress history is updated.

#### III.D.1. Wrinkle Direction

An iterative algorithm has been developed to look for a solution of Equation 9 and then check if it solves also Equation 10.

Starting with the principal stress directions that were used to test for wrinkling, the coordinate system is rotated by the corresponding angle  $\alpha$ . The shear strain  $\gamma_{xy}^u$  from Equation 9 is compared to the shear strain passed by Abaqus to the UMAT,  $\gamma_{xy}$ .

Figure 4(a) shows typical values of  $\gamma_{xy}^u$  and  $\gamma_{xy}$  plotted over  $\alpha$ . If the difference is more than some tolerance (set to  $tol = \varepsilon_{11}^p \cdot 0.001$ ) then Equation 9 is evaluated for a new trial angle  $\alpha_n$ . The first correction is  $\alpha_2 = \alpha_1 + 1^\circ$ . Thereafter  $\alpha_{n+1}$  is determined using a Newton-Raphson scheme where a line through  $\gamma_{xy}^u(\alpha_{n-1})$  and  $\gamma_{xy}^u(\alpha_n)$  is used to calculate the next estimate. This method was found to yield quick convergence in most cases (typically within 3-5 iterations). In a few cases however the Newton-Raphson solution converges to a local minimum as in Figure 4(b). If convergence isn't achieved after  $n = 10$  iterations, the range of

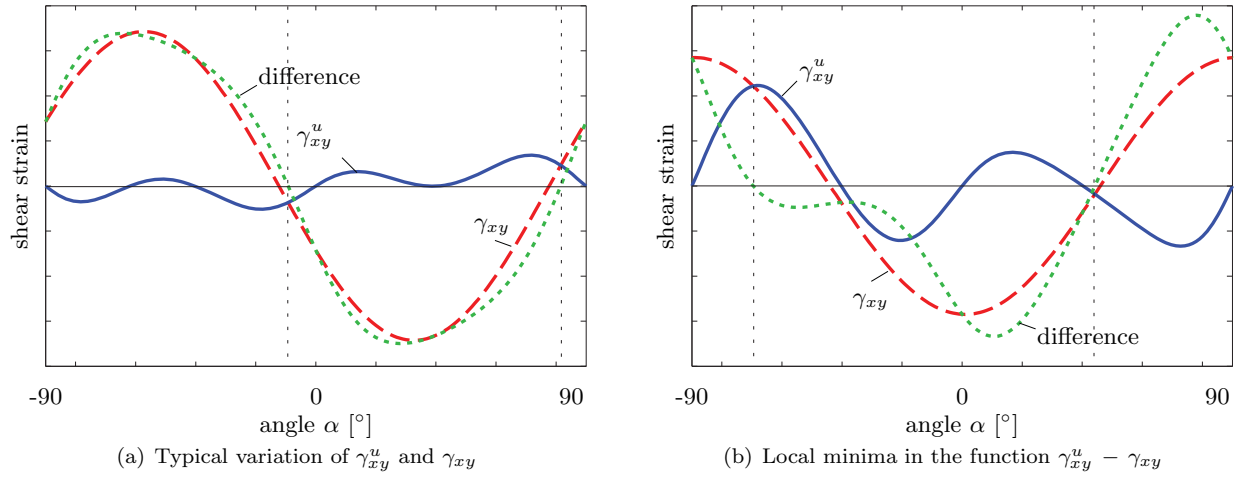


Figure 4: Typical variation of  $\gamma_{xy}^u$  and  $\gamma_{xy}$  with  $\alpha$

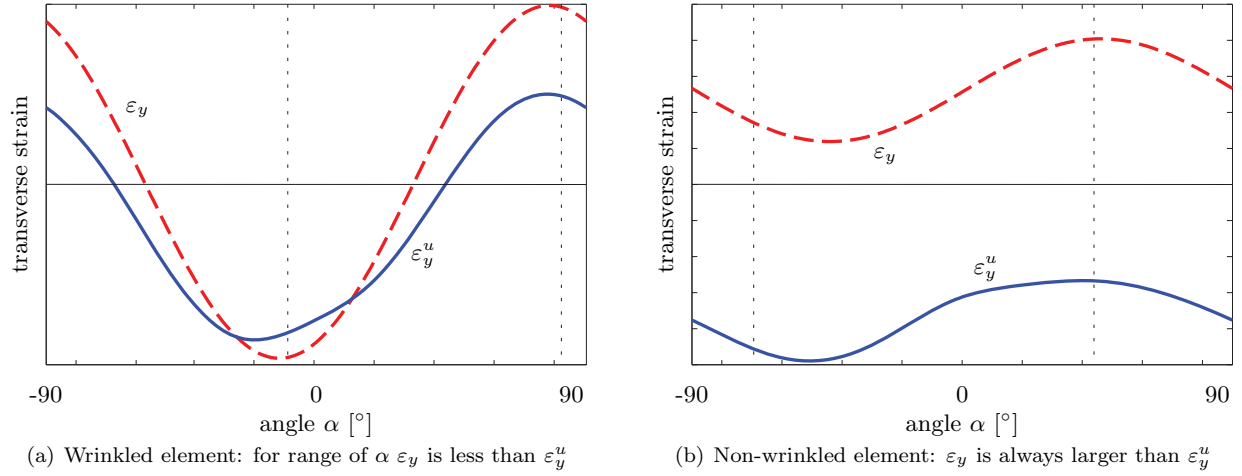


Figure 5: Typical variation of  $\epsilon_y^u$  and  $\epsilon_y$  with  $\alpha$

$\alpha_n \pm 45^\circ$  is swept in  $10^\circ$  increments. This allows the intersection of  $\gamma_{xy}^u$  and  $\gamma_{xy}$  to be narrowed down to a smaller range of  $\alpha$  and then the Newton-Raphson scheme is started again.

In Figure 4 it can be seen that there is more than one value of  $\alpha$  for which  $\gamma_{xy}^u = \gamma_{xy}$ . For each of these values the actual transverse strain  $\epsilon_y$  is compared to  $\epsilon_y^u$ , calculated from Equation 10. If wrinkling has occurred, then  $\epsilon_y^u > \epsilon_y$  for that particular  $\alpha$ . If instead  $\epsilon_y^u < \epsilon_y$  the wrong intersection has been found and the search for  $\alpha$  is repeated by starting from a value  $90^\circ$  different from the current solution. The  $\epsilon_y$  check for a wrinkled element is illustrated in Figure 5. The two vertical dashed lines in each plot mark the possible value of  $\alpha$  determined from Figure 4. If an element was falsely determined to be wrinkled,  $\epsilon_y$  is always larger than  $\epsilon_y^u$ , Figure 4(b).

Once wrinkling occurs, there exists only one solution for  $\alpha$  that satisfies the conditions for both  $\gamma_{xy}^u$  and  $\epsilon_y^u$ .<sup>7</sup> For this particular angle  $\alpha$  the strain component  $\epsilon_x$  and the shear strain component  $\gamma_{xy}$  are the actual material response to a uniaxial stress. The transverse strain component  $\epsilon_y$  from simple coordinate transformation is not the actual material strain but includes the over-contraction due to wrinkling. The implications of this difference are discussed in the next subsection.

### III.D.2. Uniaxial Viscoelastic Stress

Once the wrinkling direction is known, the coordinate system is rotated with the  $x$ -direction parallel to the direction of the wrinkles. Then the uniaxial stress is determined in an iterative procedure similar to the taut



case, Section III.C. Since the transverse and shear stresses are already known to be zero, it is sufficient to do the stress iteration for the  $x$ -direction. However, the stress history and any stresses from the previous increment still need to be considered biaxially.

Note that wrinkling has no impact on the assumptions from viscoelasticity; i.e. over the current time increment all nonlinearity coefficients are assumed to remain constant and the two terms  $g_2\sigma$  and  $\lambda\psi^\tau$  are assumed to change linearly. It is also assumed that the direction of the uniaxial stress does not change during the current time increment.

### III.D.3. Effective Elasticity Matrix

The stress-strain relationship is desired in the form

$$\Delta\sigma_i = C_{ij} \Delta\varepsilon_j \quad (13)$$

where  $C_{ij}$  is the effective elasticity matrix. For an orthotropic nonlinear viscoelastic material the components of  $C_{ij}$  are obtained from the derivatives  $\frac{\partial\sigma_i}{\partial\varepsilon_j}$ , which can be computed once the correct uniaxial stress has been found. If the coordinate system is rotated such that the  $x$ -direction is aligned with the direction of the wrinkles, Equation 13 can be written as

$$\begin{Bmatrix} \Delta\sigma_x \\ \Delta\sigma_y \\ \Delta\tau_{xy} \end{Bmatrix} = \begin{bmatrix} C_{11} & C_{12} & C_{16} \\ C_{21} & C_{22} & C_{26} \\ C_{61} & C_{62} & C_{66} \end{bmatrix} \cdot \begin{Bmatrix} \Delta\varepsilon_x \\ \Delta\varepsilon_y \\ \Delta\gamma_{xy} \end{Bmatrix} \quad (14)$$

As explained in Section III.D.1, in this particular coordinate system the strains  $\varepsilon_x$  and  $\gamma_{xy}$  are actual material strains whereas  $\varepsilon_y$  is not. Consequently any change of  $\varepsilon_y$  must not affect the resulting stresses (unless the element becomes taut again). Also, the stress is uniaxial in the  $x$ -direction and the transverse stress is zero and remains independent of any strain changes

$$\Delta\sigma_y = C_{21} \Delta\varepsilon_x + C_{22} \Delta\varepsilon_y + C_{26} \Delta\gamma_{xy} = 0 \quad (15)$$

Therefore, for the change of the material's actual transverse strain  $\Delta\varepsilon_y$  we can write

$$\Delta\varepsilon_y = -\frac{C_{21}}{C_{22}} \Delta\varepsilon_x - \frac{C_{26}}{C_{22}} \Delta\gamma_{xy} \quad (16)$$

By eliminating  $\Delta\varepsilon_y$  in Equation 14 the expressions for  $\Delta\sigma_x$  and  $\Delta\tau_{xy}$  can be rewritten as:

$$\Delta\sigma_x = \left[ C_{11} - \frac{C_{21}^2}{C_{22}} \right] \Delta\varepsilon_x + \left[ C_{16} - \frac{C_{12}C_{26}}{C_{22}} \right] \Delta\gamma_{xy} \quad (17)$$

$$\Delta\tau_{xy} = \left[ C_{61} - \frac{C_{62}C_{21}}{C_{22}} \right] \Delta\varepsilon_x + \left[ C_{66} - \frac{C_{26}^2}{C_{22}} \right] \Delta\gamma_{xy} \quad (18)$$

The remaining entries of the effective elasticity matrix are zero, because of the additional requirement of keeping  $\sigma_y$  independent of any strain changes. In conclusion,

$$C_{ij} = \begin{bmatrix} C_{11} - \frac{C_{21}^2}{C_{22}} & 0 & C_{16} - \frac{C_{12}C_{26}}{C_{22}} \\ 0 & 0 & 0 \\ C_{61} - \frac{C_{62}C_{21}}{C_{22}} & 0 & C_{66} - \frac{C_{26}^2}{C_{22}} \end{bmatrix} \quad (19)$$

For an orthotropic material the individual components of the above matrix can be derived from a standard coordinate transformation.

In a displacement based finite element algorithm using the Newton-Raphson method the next strain increment would be provided together with a stress estimation based on Equation 19. Since the angle of the wrinkles for Equation 19 was chosen based on a particular ratio  $\varepsilon_x/\gamma_{xy}$ , the change of shear stress  $\Delta\tau_{xy}$  is zero only if the ratio of  $\Delta\varepsilon_x$  over  $\Delta\gamma_{xy}$  remains the same. Otherwise a small shear stress component  $\Delta\tau_{xy}$  appears and causes a small rotation of the wrinkle orientation compared to the previous increment.

### III.E. Slack Membranes

If an element is found to be slack the stresses are set to zero and a zero effective elasticity matrix is returned to Abaqus. The stress history is updated with zero stresses for the duration of the current time increment (viscoelastic recovery).

## IV. Creep Strain Measurements

### IV.A. Balloon Structure

Preliminary experiments on two and four meter diameter balloon models had shown that time-dependent strain measurements should be carried out on a pristine and undamaged structure, without any pre-existing plastic deformation. Aerostar International, a subsidiary of Raven Industries, provided a new balloon made of 0.038 mm thick SF430 film. The balloon was a 48-lobe pumpkin balloon with nominally 4 meter diameter (height 2.396 m). The lobes had constant radius design (lobe radius 157 mm, lobe angle at equator  $112^\circ$ ).<sup>17</sup>



Figure 6: 4 m diameter test balloon, 48 lobes, constant radius design

The lobe cutting pattern in Table 2 defines the half gore width and its boundary becomes the seam edge ([www.aerostar.com/aerospace.htm](http://www.aerostar.com/aerospace.htm)). The total length of the center line,  $l = 5242.56$  mm, includes the end-fitting radius of 138 mm. The total side length of the cutting pattern is 5282 mm. Figure 7 shows a plot of the cutting pattern (blue line) in comparison to the tendon distance of a "flat lobe" balloon where the lobes span across meridional lines lying on an isotenoid. Figure 8(a) shows a cross-section of a seal assembly with the two adjacent gores spread out at the bottom of the figure. The schematic diagram in Figure 8(b) shows the individual film layers with dimensions in millimeters. The layers labeled ① and ② are two adjacent gores. Their overlap region is labeled ④. The two layers labeled ⑤ are part of the tendon assembly and come preassembled with the tendon. Label ③ marks a protective layer placed on top of the lay-up for welding.

The gore tips are sealed by the apex and base fittings, Figure 9. Each end-fitting consists of one ring (inside the balloon), a circular plate (outside the balloon) with a diameter of 276 mm and another ring (outside the balloon) with 48 pins (at  $r = 126$  mm) for individual attachment of the tendons by so-called Brummel splices. In this knotting technique the end of the rope is braided into itself after forming a loop around one of the pins. In order to allow the tendon attachment to the end-fitting, they are detached from the gore seals about 320 mm before reaching the end-fitting. The end-fittings also provide gas inlets and a mounting suspension.

Smith and Cathey<sup>17</sup> have reported that measurements during manufacturing had shown difficulties in accurately achieving the small gore width towards the top and bottom apex. Concerns about material failure due to local stress concentrations were dealt with by reinforcing this area with a tape collar.

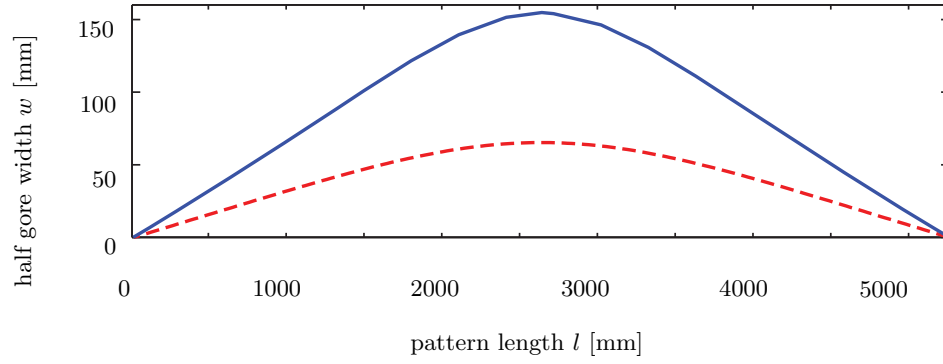


Figure 7: Cutting pattern of 4 m balloon with half gore width (blue) vs. half tendon distance of a smooth isotenoid (red)

Table 2: Gore cutting pattern including end-fitting, half width  $w$  measured to blue lines in Figure 7 and 8(b)

$l$ [mm]	$w$ [mm]	$l$ [mm]	$w$ [mm]	$l$ [mm]	$w$ [mm]
0.00	0.00	1932.43	130.81	3761.23	100.97
103.63	6.73	2237.23	146.30	4066.03	79.50
408.43	26.80	2542.03	154.05	4370.83	58.17
713.23	47.37	2618.23	154.81	4675.63	37.47
1018.03	68.33	2846.83	151.51	4980.43	17.15
1322.83	89.79	3151.63	139.57	5138.93	6.73
1627.63	111.00	3456.43	121.67	5242.56	0.00

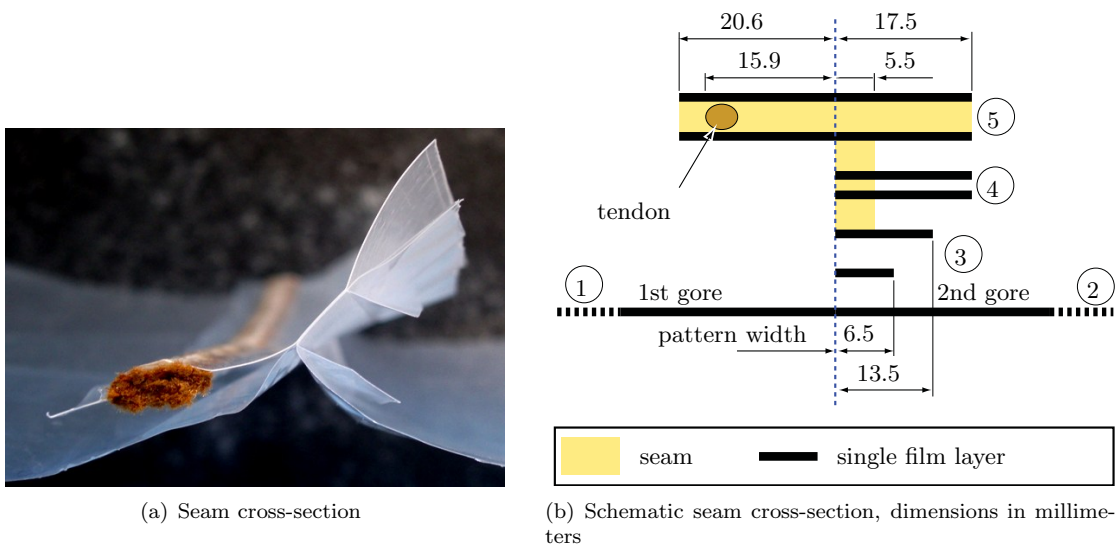


Figure 8: Seam close-up view with various film layers



Figure 9: End-fitting

## IV.B. Experimental Technique

Accurate experimental measurements on membrane structures require the use of non-contact techniques. An accurate non-contact method for strain and shape measurements has been developed based on photogrammetry,<sup>2</sup> which allows the measurement of points in three-dimensional space. The method requires an object to be photographed from different directions. Points of interest (targets) are then marked on these photos and interrelated. To provide a measure of accuracy and error minimization each of these targets needs to be seen on at least three photos. For higher accuracy it is advisable to use a set of four or more photos. Photo processing was done with the commercial photogrammetry software PhotoModeler 6.1. The three-dimensional coordinates of sets of target points, at several time steps, were analysed using Matlab scripts to determine the overall shape of the balloon and the strain variation in selected regions of the balloon surface.

### IV.B.1. Camera Setup

For time-dependent measurements all photos in a set need to be taken within a few seconds. This degree of synchronization is adequate for the slow movement of the targets due to viscoelasticity. Olympus SP-350 digital cameras (8.0 Mpixel resolution) were connect via USB ports to a personal computer. Olympus publishes a Software Developer Kit (SDK) for the SP-350 camera model to support USB control, and a camera controller shareware based on SDK V3.4 is distributed by Pine Tree Computing LLC.

Local creep strain measurements were done with four cameras mounted in front of the target area, Figure 10. Similarly, balloon shape measurements were done with a set of six cameras viewing over half of the balloon's surface.

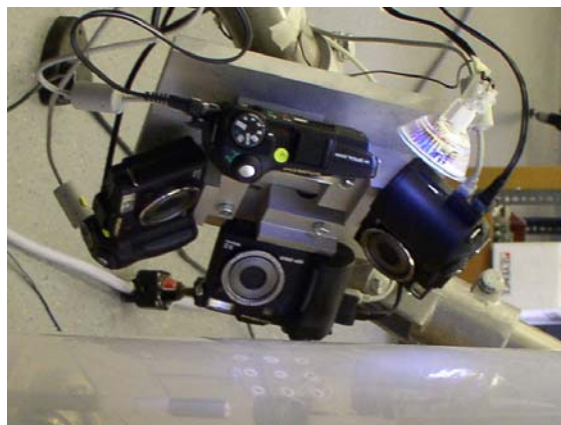
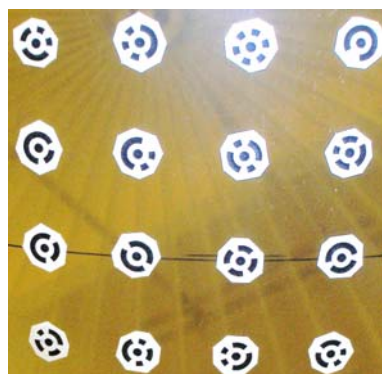


Figure 10: Four cameras for close-up creep strain measurement and LED light attached to a plate

#### IV.B.2. Targets

PhotoModeler provides coded targets that allow unique ID numbers to be assigned to each target. A 12 bit code in the form of ring sections around a circular target allows for 161 unique targets. While the coding increases the size of a target it also reduces processing time considerably. Coded targets are marked, recognized and referenced automatically by the software.



(a) Local measurement spot with 16 targets



(b) Targets for meridional measurement together with two reference targets (attached to a beam)

Figure 11: Targets distribution

For the strain measurements, three different lobes of the balloon were equipped with targets at the equator and at one quarter of the meridional length. These targets covered a  $40 \times 80$  mm rectangular region with 15 targets at the equator, and a  $60 \times 60$  mm square region with 16 targets at a quarter, with a nominal target distance of 20 mm, Figure 11(a).

For the meridional shape measurements, five lobe centerlines were equipped with targets nominally 100 mm apart, Figure 11(b). The centerline was defined in this context as the meridional line halfway between two tendons and was terminated with targets on the top and base end-fittings at  $r=105$  mm.

Shape measurements along the balloon equator were done with targets on 24 lobes around half the circumference of the balloon. The equator target positions were defined by measuring a constant arc-length along the tendons from the top end-fitting, after pressurizing the balloon. One target on each lobe was then attached half way between pairs of adjacent tendons. In addition PhotoModeler required targets distributed over the balloon surface for processing; hence on each lobe another two targets were attached 60 cm above and below the equator targets.

Two additional targets (not attached to the surface) were positioned at a distance of 44.59 mm and 891 mm, respectively, and were included in at least 3 photographs to provide a reference length for photogrammetry processing.

#### IV.B.3. Experimental Setup

The top end-fitting of the balloon was supported by a rope going over a set of two pulleys attached to the ceiling and was initially free to rotate and translate. The bottom end-fitting was equipped with a Sensor Technics pressure transducer (Model CTEM70025GY7) with a maximum pressure of 2500 Pa. An air line was attached to the top end-fitting to minimize any additional loading on the balloon due to the weight of the air line hose.

Rigid-body movements of the balloon during the tests were minimized by attaching three balloon seams to strings running over pulleys attached to vertical poles and carrying 50 g weights. Two of the strings restrained translational degrees of freedom and one restrained rotation, Figure 12. The counterweights were chosen to be sufficiently small to prevent visible deformation of the balloon and any measurements were carried out away from the string attachments.



For the strain measurements the four cameras were mounted on an adjustable platform that kept the cameras close to the surface at all pressures. For the balloon shape measurements six cameras were mounted in fixed positions at distances of 1-3 m from the balloon. With this arrangement it was possible to cover about half the balloon circumference either horizontally (equator shape) or vertically (meridional shape).



Figure 12: Experimental setup for local creep strain measurements; left circle: cameras mounted on a trolley-winch assembly, right circle: string with counterweight going over pulley

#### IV.B.4. Experimental Procedure

At the beginning of each test the balloon was filled with air to a pressure of 15-20 Pa. The pressure was held constant for 10-60 min, depending on how much time was required for preparations, and a reference set of photos was taken. Then, the differential pressure was increased in four steps to 120, 250, 500 and 700 Pa. Each pressure level was held nominally for 30 minutes, Figure 13. Temperature and loading were monitored throughout the experiment.

Under loading the movement of the coded targets was recorded by taking sets of photos, initially at intervals of five seconds to capture enough detail of the deformation. Gradually over the duration of a pressure-hold period these intervals were increased up to 60 seconds, but whenever the nominal pressure was about to be changed the smaller intervals were resumed. The laboratory temperature was monitored with a digital thermometer and was found to be fairly constant with a variation of less than  $0.3^{\circ}\text{C}$  over the duration of each experiment.

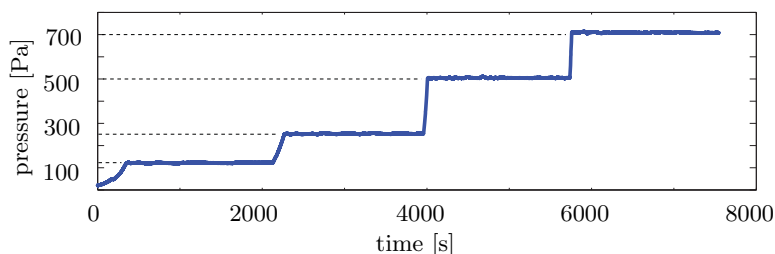


Figure 13: Record of pressure vs. time during balloon experiments

#### IV.B.5. Processing of Experimental Data

After the photos had been processed with the photogrammetry software, the coordinates of the targets in a random sequence, called a point-cloud, were known at each time step, including the initial reference.

All distances were computed using the actual arc length on the balloon surface rather than the direct distance. Due to the distribution of the targets for creep strain measurements it would have been easy to estimate the local radius of curvature of a circle defined by three points that were aligned on the initial flat gore. However, in practice these targets were never perfectly aligned and hence the resulting radius of curvature would not be accurate. Therefore a more general analysis was carried out, as follows.

It was assumed that any surface can be represented locally by a general second-order polynomial

$$z = a_1 + a_2x + a_3y + a_4xy + a_5x^2 + a_6y^2 \quad (20)$$

where the coefficients  $a_i$  were fitted by least squares to the point-cloud in the global coordinate system. Then the coordinates were transformed into a local system with the origin at the center target and the  $z$ -axis aligned with the surface normal. In this local coordinate system a new polynomial was fitted to the point-cloud

$$z = b_1x^2 + 2b_2xy + b_3y^2 \quad (21)$$

and the principal curvatures were determined. Two assumptions were made for the principal curvatures: firstly, they are aligned with the meridional and hoop directions of the balloon, and secondly they do not change over the small area of the targets. Hence, the surface section in Figure 14 is a circular arc and the radius of curvature  $r$  is either of the principal radii.

The unique ID numbers of the coded targets were then used to identify pairs of adjacent targets that are "aligned" in the meridional or hoop direction. The length  $s$  of a circular section between two targets is

$$s = 2r \arcsin \frac{\xi}{2r} \quad (22)$$

where  $1/r$  is the principal curvature in the meridional or hoop direction and  $\xi$  is the direct distance between two adjacent targets, Figure 14.

The time-dependent strains between these pairs of targets were computed from the initial reference distance and the time-dependent distance.

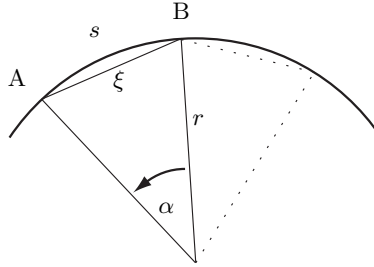


Figure 14: Circular arc through two adjacent targets

The balloon shape measurements were processed as follows. For the lobe shape measurements the target numbers for each lobe were manually selected from the point-cloud. A plane was defined by the two end-fitting targets and the target closest to the equator. The coordinates of these target points were transformed such that the line between the targets on the end-fittings lay on the plane and was parallel to the balloon axis. Since the balloon axis lies at the intersection of these planes, the in-plane coordinates describe the profile of the meridian that was marked half-way between the tendons. Since the meridional curves run between the top and the bottom end-fittings, the end-fitting distance determines the balloon height at different pressures. For the measurement of the equator the target numbers along the equator were selected manually to extract the equatorial coordinates from the point-cloud. First a plane was fitted to the three-dimensional coordinates of this set of points by a least squares fit. Then, the coordinates were transformed into a cylindrical coordinate system with the  $z$ -direction perpendicular to the fitted plane (and parallel to the balloon axis). The balloon center was then determined by finding the center of the best-fit circle to the set of equatorial points. The results give insight into radial and out-of-plane deviations from this circle.

#### IV.B.6. Accuracy of Strain Measurements

The total accuracy of the creep strain measurement is affected by two factors; the photogrammetry method and the strain calculation that is based on the local representation of the surface by a quadratic polynomial.

The accuracy of the photogrammetry method is influenced by camera positions, resolution, calibration, target distribution and how well the targets are marked in the photographs. The resulting precision describes the spread of a measured target coordinate and can be used as an estimate for accuracy if gross and systematic errors are neglected. The precision values provided by Photomodeler for an individual target are equal to two standard deviations, assuming a normal Gaussian probability curve (68%). The precision of photogrammetry projects depends highly on the resolution and the size of the measured object.

For local creep strain measurements where each photograph had a field of view of up to 150 mm, the precision of each target was typically in the order of 0.01 mm with a worst case limit of 0.04 mm. The photos for balloon shape measurements covered areas up to 5 m wide and hence precision values were considerably worse. Considering the size of the whole balloon though (4 m diameter, 2.396 m height), the measurements had a precision typically of 1.2 to 2.5 mm.

To assess the accuracy of the strain calculation method, a set of nine targets, 20 mm apart on a sphere with radius  $r$  were generated in Matlab with

$$r^2 = (x - x_0)^2 + (y - y_0)^2 + (z - z_0)^2 \quad (23)$$

where  $x_0, y_0, z_0$  are the coordinates of the center of the sphere. Three different radii of the sphere were considered (see Table 3). The arc length  $S$  between two adjacent targets was then determined using the analysis method presented above. Comparing this value to the exact arc-length revealed small deviations  $\Delta S$  that would result in a strain calculation error  $\Delta\epsilon$ , Table 3.

Table 3: Strain calculation error between two targets (20 mm apart) on locally spherical surface

radius [mm]	$\Delta S$ [mm]	error $\Delta\epsilon$ [%]
150	$2.44 \times 10^{-4}$	0.0012
157	$2.02 \times 10^{-4}$	0.0010
440	$3.21 \times 10^{-6}$	$1.6 \times 10^{-5}$

It was found that the arc length variation  $\Delta S$  due to the polynomial fit is very small in comparison to the typical and worst-case precision of the target coordinates obtained from photogrammetry (0.01 and 0.04 mm). Hence it can be concluded that the strain measurement accuracy is determined by the error in the photogrammetry measurements. Since the target distance is 20 mm the strain measurement error can then be stated as typically 0.05% (worst 0.2%).

## V. Symmetric Finite Element Model of a Lobe

### V.A. Abaqus Model Description

The balloon described in Section IV.A had  $n = 48$  lobes and took an approximately 48-fold symmetric shape when it was pressurized. Since the cutting pattern of each gore has mirror symmetry across the centerline, by neglecting the details of the seams and hence assuming that the tendons run along the edges of the cutting pattern, only half of a lobe needs to be analysed.

#### V.A.1. Mesh and Element Types

The balloon lobes become very narrow towards the end-fittings and sometimes adjacent lobes come into contact in the equator area. Hence, meshes with large numbers of elements (up to 36000) were used to represent the lobe. Because the user-defined subroutine has to be called at each integration point, lower order elements were preferred for their lower computational cost. It was found that the generally smooth surface of a lobe can be well represented with linear elements (M3D3, one integration point); in areas with locally higher surface curvature the mesh was further refined. Triangular elements were found convenient for creating unstructured meshes that are divided in multiple domains with different mesh resolutions. The



element properties were defined with `*membrane section` and the material directions with `*orientation`. A constant thickness of  $38\ \mu\text{m}$  and the Poisson's ratio of 0.5 (incompressibility) were assigned. The material's machine direction was oriented along the length of the gore (meridional) and the material's transverse direction with the hoop direction.

The balloon has a more curved and highly wrinkled lobe shape along the tendons and at low pressure ( $p < 150\ \text{Pa}$ ). A finer mesh is also required in the equator area in order to model contact between different lobes. The surface was subdivided into 4 domains with different resolution; two end-fitting areas (328 mm long) with element side lengths of 2-4.5 mm (each 756 elements), and a narrow strip (3-33 mm wide, 2150 mm long) along the tendon, centered at the equator with 2-3 mm sidelength (17206 elements). The remaining area was meshed with a finer resolution (minimum 2 mm) towards the tendons and a coarser resolution towards the gore center (maximum  $l = 30\ \text{mm}$  at the center of the gore at the equator), resulting in 17821 elements. The mesh was generated in Abaqus CAE and had a total of 19234 nodes and 36539 elements.

The tendons were modeled with (T3D2) two-node truss elements connected to the nodes along the boundary of the membrane mesh. The element's cross-section was defined with `*solid section`.

### V.A.2. Boundary Conditions and Constraints

One half of a single lobe was modeled with its centerline lying in the  $xz$ -plane. The 48-fold symmetry of the balloon was then enforced by constraining the edge nodes of the cutting pattern to remain within the symmetry planes, Figure 15. This constraint was formulated with `*equation` where any displacement component in the  $y$ -direction equals the corresponding  $x$ -component times  $\tan \frac{\pi}{n}$ . However, the `*equation` constraint needs to be part of the model definition and cannot be modified during the simulation. In order to allow activation of the constraint at a later stage (see Section V.A.4) an additional set of dummy nodes was introduced, one for each node along the edge of the cutting pattern, and the constraint written as

$$-\Delta y_{tendon} + \Delta x_{tendon} \tan \frac{\pi}{2} + \Delta y_{dummy} = 0 \quad (24)$$

where the subscript *tendon* denotes nodes along the cutting pattern edge and the subscript *dummy* denotes the dummy nodes. If  $y_{dummy}$  in Equation 24 is unconstrained,  $x_{tendon}$  and  $y_{tendon}$  can move independently. The centerline nodes were simply confined to the  $xz$ -plane.

The end-fittings were assumed rigid and modeled through boundary conditions only. Therefore the boundary nodes along an end-fitting were coupled to a dummy node using `*kinematic coupling`. One end-fitting was held in place and the other one was allowed to move in the  $z$ -direction only.

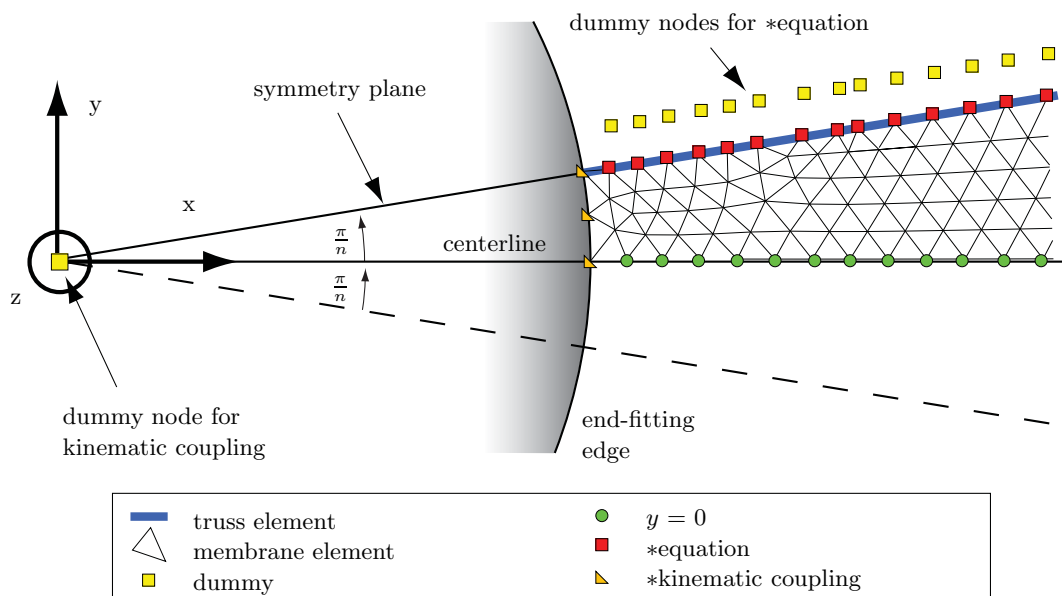


Figure 15: End-fitting area with boundary conditions

The distribution of the coupling and equation constraints is illustrated in Figure 15. The origin of the coordinate system is at the center of the end-fitting. The angle between the symmetry plane and the centerline plane is  $\pi/n$ .

The balloon's symmetry planes may not be penetrated by the balloon film, Figure 16. This can be prevented by the following contact formulation. The command `*contact pair` identifies a pair of surfaces (master and slave) that may not intersect. With the `*surface` command the master surface was defined as a rigid plane coinciding with the symmetry plane and the slave surface was defined by a set of nodes with a distance of less than 30 mm from the edge of the cutting pattern. The relative motion between the contact surfaces was defined as frictionless.

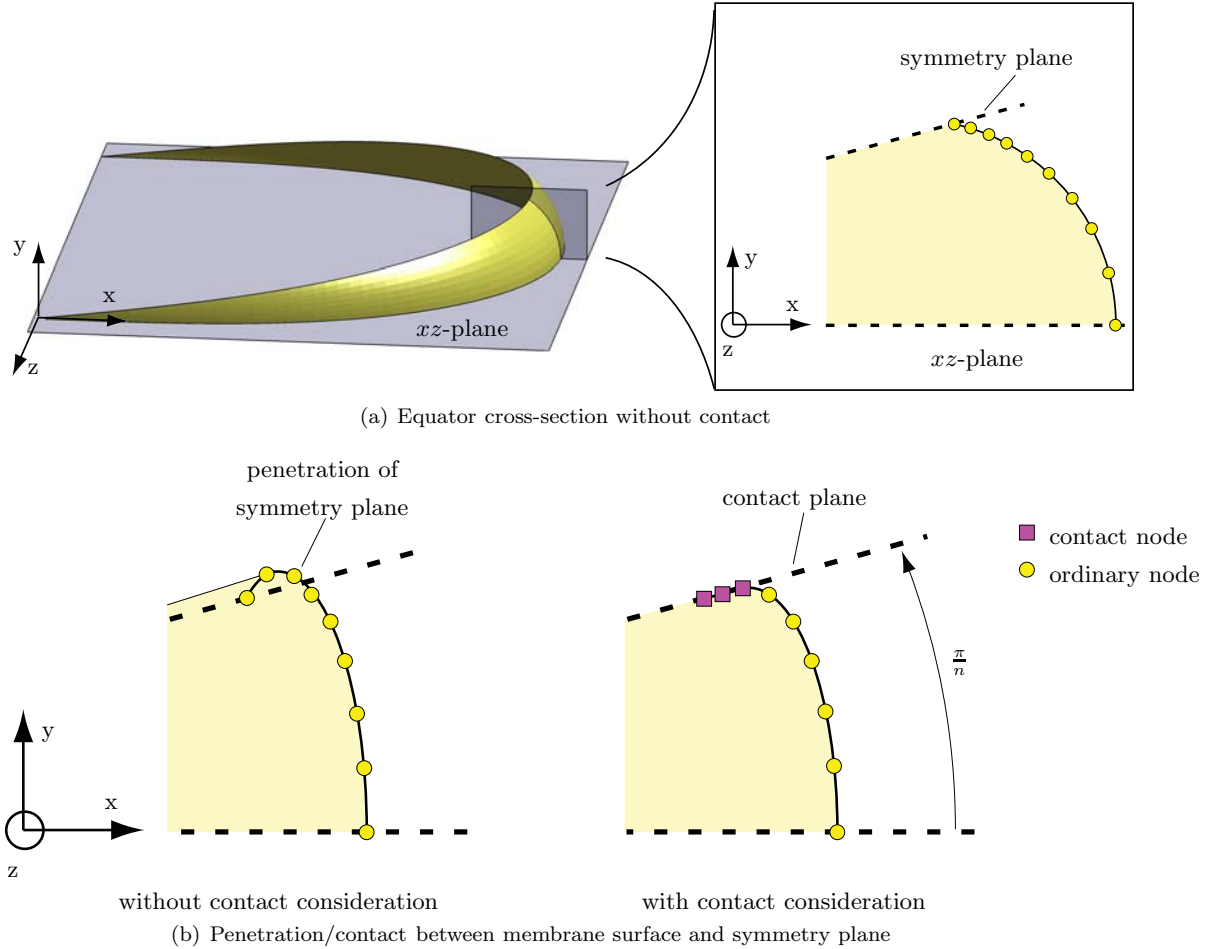


Figure 16: Contact constraint at equator cross-section

### V.A.3. Numerical Convergence

Abaqus breaks the simulation into a number of time increments and finds the approximate equilibrium configuration at the end of each increment using the Newton-Raphson method. For equilibrium the net force acting at every node must be zero, hence the internal forces  $I$  and the external forces  $P$  must be in equilibrium. The nonlinear response to a small load increment  $\Delta P$  is used together with the tangent stiffness matrix to compute a displacement correction. Based on the displacement correction the internal forces  $I$  are determined and the difference between  $P$  and  $I$  gives a force residual

$$R = P - I \quad (25)$$

Convergence is achieved when the residual  $R$  is less than a defined tolerance (default: 0.5% of time average force). If the solution hasn't converged Abaqus performs another iteration with an updated tangent stiffness

matrix and a new displacement correction. If necessary, Abaqus automatically cuts back the increment size and makes another attempt. These convergence checks at the end of every increment continuously guarantee the accuracy of the solution.

Convergence difficulties were observed either due to a geometrical instability (e.g. a sudden out-of-plane movement of the membrane elements), or due to material "softening" causing zero stiffness due to wrinkling. The user-defined subroutine presented in Section III prevents local buckling caused by compressive stresses in membranes. There are two approaches to help a solution to converge:

1. Artificial damping forces can be introduced with the **stabilize** parameter;
2. Existing membrane elements can be overlayed with a set of elements that maintain a very small artificial stiffness.

### Artificial Damping Forces

The **stabilize** parameter introduces artificial forces at nodes that undergo high acceleration during an increment. These forces are calculated from

$$F_{stabilize} = cM^*v \quad (26)$$

where  $M^*$  is an artificial mass matrix calculated assuming unity density,  $c$  is a damping factor,  $v = \Delta u / \Delta t$  is the vector of nodal velocities and  $\Delta t$  is the current time increment. These forces introduce an error that needs to be kept to a minimum. In the present study the value of  $c$  was specified in the Abaqus input file with the parameter **Factor**. Instead of the default value,  $c = 2 \times 10^{-4}$  1/s,  $c$  ranged from  $10^{-33}$  to  $10^{-20}$  1/s with maximum forces of 0.3393 N.

When membranes undergo large out-of-plane displacements artificial damping may inhibit node movements and prevent the membrane structure from taking its actual equilibrium shape. If relatively high damping forces are required to control the solution, often they can be reduced over several restart steps with gradually decreasing damping factors. This approach is acceptable for time-independent material behavior, however in the viscoelastic regime errors due to damping forces would have a direct impact on the results at a given time and hence should be kept very small values at all times. Hence, in the present study the **stabilize** parameter has been used only to help against convergence difficulties observed during the initial lobe forming when no viscoelastic effects were considered (see Section V.A.4).

### Material Softening

In a preliminary study a uniform cylinder model that was wrinkled in the axial direction was investigated and it was found that material softening caused by zero stiffness in the wrinkling direction can sometimes lead to convergence difficulties. In the case of balloon lobes this issue was observed especially in heavily wrinkled areas, where node positions were not well determined. In this case the solver keeps correcting the solution by introducing infinitesimally small movements without any impact on the strains or stresses.

This behavior can be greatly improved by overlaying the wrinkled membrane with low-stiffness elastic elements to provide a small artificial stiffness in the wrinkling direction. Adding a small prestress to the overlayed elements determines the node positions due to very small element stresses that remain always positive. The overlayed membrane elements were isotropic with Young's modulus  $E = 1$  MPa. The prestress was 0.05 MPa in meridional and 0.16 MPa in circumferential direction. As a result convergence was considerably improved. On the downside in a heavily wrinkled area these small forces cause a uniform redistribution of the membrane that may not be observed in an experiment.

#### V.A.4. Lobe Forming Process

Since the lobes are made from flat sheets of thin plastic, the material has to stretch in order to produce a lobed shape with positive Gaussian curvature. In a real balloon the doubly-curved shape is obtained gradually during inflation of an initially loosely hanging structure with many folds. Numerically, this lobe forming process was approximated by constraining the lobe boundaries to lie within their meridional symmetry planes while the membrane forming the lobe is wrinkled or even slack to accommodate possibly superfluous material. This was done in the following sequence of steps:

1. Initial pressurization with fully constrained boundaries;
2. Movement of the boundary nodes onto balloon symmetry planes;

3. Release of boundary nodes in the symmetry planes;
4. Decrease pressure to some very low value, e.g. 5 Pa.

The lobe forming process was carried out in a sufficiently short period of time that the material's response is still purely elastic. This means the total time required for the above four steps should be less than three orders of magnitude before the time at which viscoelastic material behavior is defined. Here the lobe forming process was completed at  $t = 10^{-22}$  s. This means that potentially very high stresses during lobe forming occur only in the elastic regime and have no effect on the time-dependent material behavior or stress history. In fact, only the stresses and strains that occur after the beginning of the viscoelastic time domain (i.e.  $t = 1.6 \times 10^{-19}$  s, see Section II.B.2) matter.

The process started from the flat cutting pattern of the lobe. The pattern was mapped onto a cylindrical surface defined by the generator of the isotenoid surface. The length of this generator between balloon apex and base matched exactly the length of the pattern's centerline. Hence, every length coordinate along the pattern corresponds to a pair of  $x$  and  $z$  coordinates on the generator. The  $y$  coordinates (pattern width) remained unchanged. Note that in this configuration the edge of the pattern generally does not lie on the balloon's symmetry planes, if the pattern width doesn't correspond to the tendon distance of an isotenoid.

In the **first step** all of the boundary and dummy nodes were held fixed and an initial pressure of 50 Pa was applied. In the **second step** the boundary nodes were moved in the  $y$ -direction onto the balloon's symmetry planes. Therefore the dummy nodes were moved in the  $y$ -direction while  $x_{tendon}$  was held fixed and Equation 24 becomes

$$\Delta y_{tendon} = \Delta y_{dummy} \quad (27)$$

In the **third step** the boundary nodes were allowed to move freely in the meridional symmetry planes to find their equilibrium configuration. The constraints on  $x_{tendon}$  were deleted and the dummy nodes were held fixed for the remainder of the simulation, thus Equation 24 becomes:

$$\Delta y_{tendon} = \Delta x_{tendon} \tan \frac{\pi}{2} \quad (28)$$

In addition only the top end-fitting was held in place while the bottom end-fitting was free to move along the balloon axis. Finally the **fourth step** decreased the pressure load to a lower value, such as 20 Pa. This pressure value is low enough to ensure low membrane stresses at the beginning of the viscoelastic analysis. Ideally the viscoelastic simulation should start with no pressure applied. However, when the pressure is decreased most of the membrane becomes highly wrinkled (zero hoop stress), which results in a very small time average force, such as 0.0157 N ( $p = 20$  Pa). Since the default convergence tolerance is 0.5% of the time average force; lower pressure values caused convergence difficulties that could only be overcome by increasing the residual error tolerance. At these lower pressures it is important to use the contact formulation to prevent intersection of the membrane and the symmetry planes. Note that this step ended with all stabilize forces fully removed.

#### V.A.5. Viscoelastic Analysis Steps

Once the fourth step had been completed and any damping forces fully removed, the viscoelastic analysis was started. The temperature was set to the measured lab temperature ( $T = 296$  K) at the beginning of the

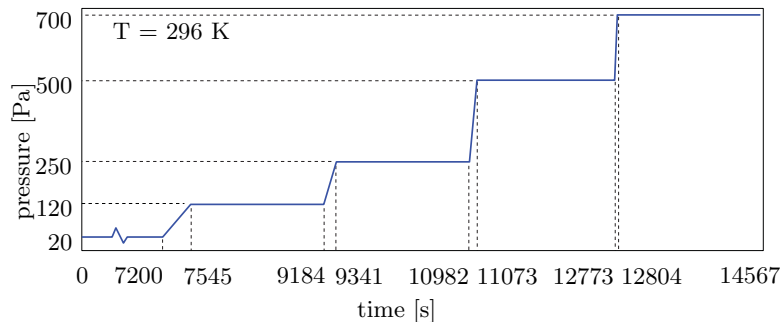


Figure 17: Pressure record modeled with ramp and step functions

analysis and assumed to be constant throughout the test. The pressure record over time was approximated as shown in Figure 17.

The first step started with an increment size of  $\Delta t = 10^{-22}$  s and depending on the convergence Abaqus automatically increased the time increment size ( $\Delta t_{max} = 200$  s) until the total hold of 2 h had been completed. Thereafter each analysis step started with  $\Delta t = 1$  s and the time increment was automatically increased up to  $\Delta t_{max} = 200$  s, but never more than 10% of the total time of an analysis step.

A large portion of the required computing time was spent on the 4th lobe forming step and the initial 2 h low pressure hold. Hence, these parts of the simulation were divided into several smaller analysis steps depending on the observed convergence behavior. If necessary the error residual tolerance was then controlled in these smaller analysis steps. As previously mentioned the low pressure load of 20 or 5 Pa resulted in very small time average forces. Thus the default residual error tolerances of only  $7.87 \times 10^{-5}$  made numerical convergence impossible. In order to achieve convergence the residual tolerance had to be increased. A suitable tolerance was temporarily chosen for each individual analysis step resulting in maximum tolerances of  $2.72 \times 10^{-2}$  N. Once a higher pressure had been applied, the error residual tolerance was reset to its default of 0.5% of the time average force.

## VI. Results

Figure 18 shows the strain distribution in a lobe at five different pressure levels, at the end of each pressure hold. This means that an initial pressure of 20 Pa has been maintained for 2 h and pressures of 120, 250, 500 and 700 Pa for 27-29 min. Half of the lobe has been plotted for each strain component. At low pressures of 20 and 120 Pa a large area of the lobe is heavily wrinkled in the hoop direction and the surface contracts by up to -13.5 %. At the end of the 250 Pa hold the wrinkles have disappeared.

In Figure 19 the corresponding stress distribution has been plotted. At 20 Pa the hoop stresses are practically zero. Peak stresses occur next to the apex and base end-fittings and haven't fully relaxed after 2 h. At 120 Pa the meridional stress increases, while the hoop stresses are still largely zero due to wrinkles. The stresses become non-zero in the whole gore at 250 Pa. Note how up to 250 Pa the maximum meridional stresses have increased to over 5 MPa whereas further pressurisation to 500 and 700 Pa results in only 1 MPa additional stress.

Figure 20 shows the change in strain distribution during a constant pressure period; the strains have been plotted at the beginning and the end of the 27 min pressure hold at 120 Pa. Meridional strains increase in particular at the equator (by almost 1 %) and due to Poisson's effects the amount of wrinkling in the hoop direction decreases. The corresponding change in the stress distribution is plotted in Figure 21. The material redistribution causes the two initially separated stress peaks to shift in the direction of the equator. The hoop stresses are still largely zero due to wrinkling.

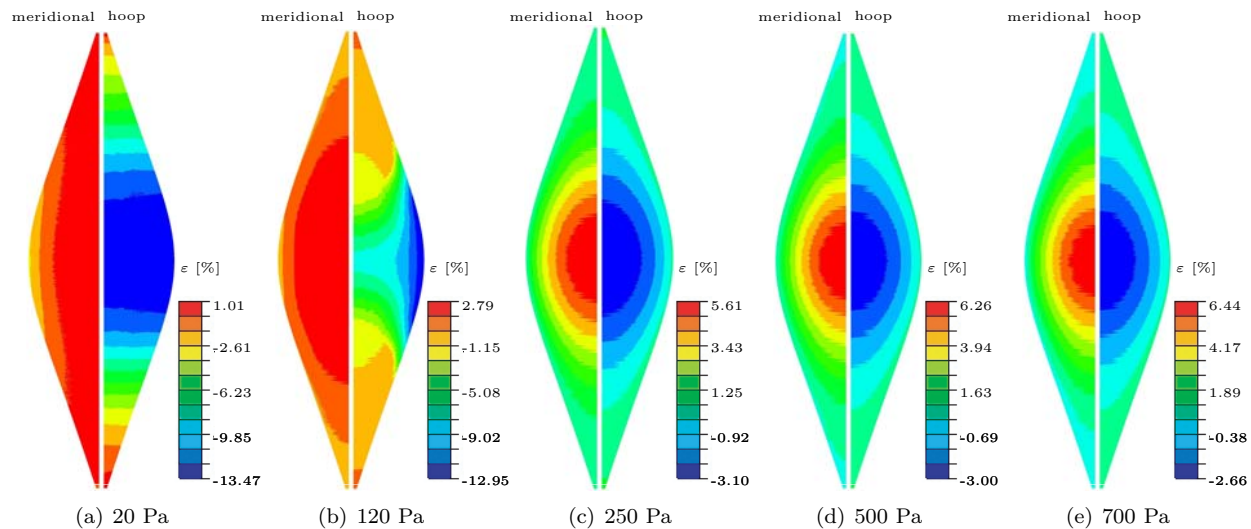


Figure 18: Strain distribution at the end of each pressure hold

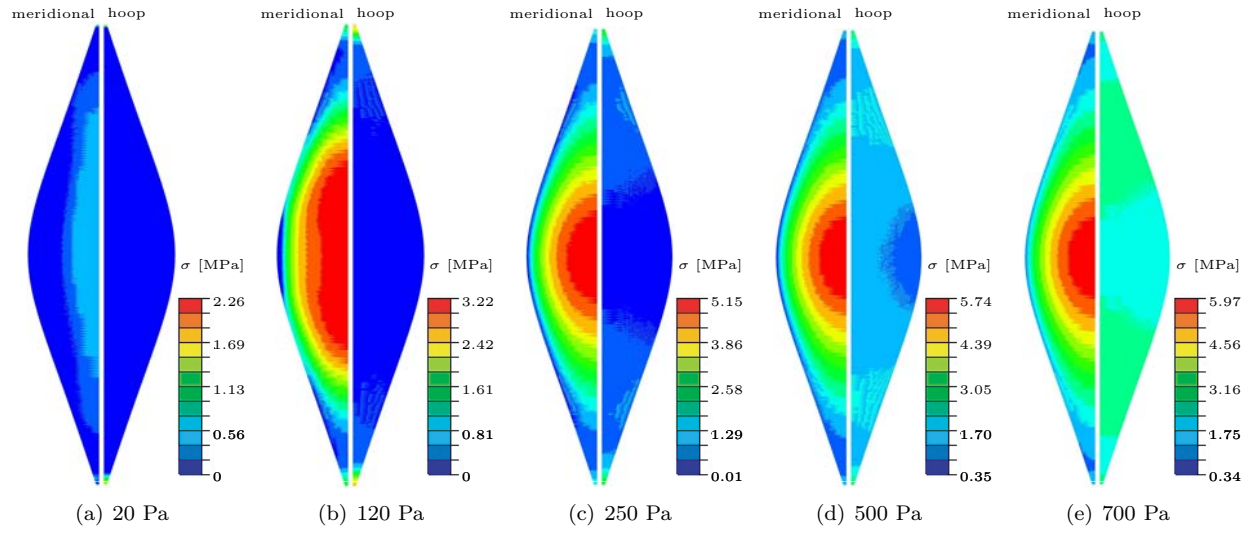


Figure 19: Stress distribution at the end of each pressure hold

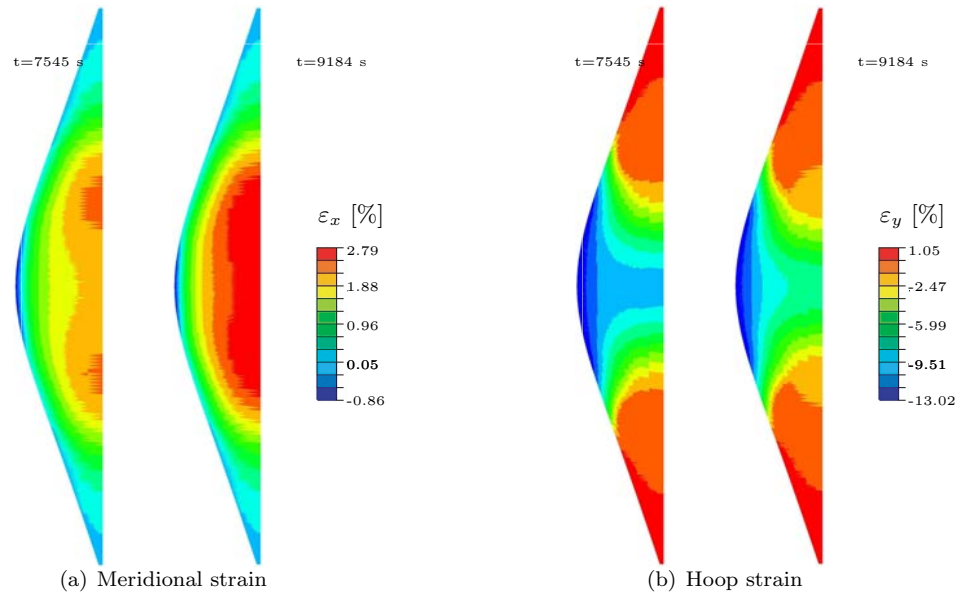


Figure 20: Change of strain distribution during period of constant pressure; before and after 27 min at 120 Pa

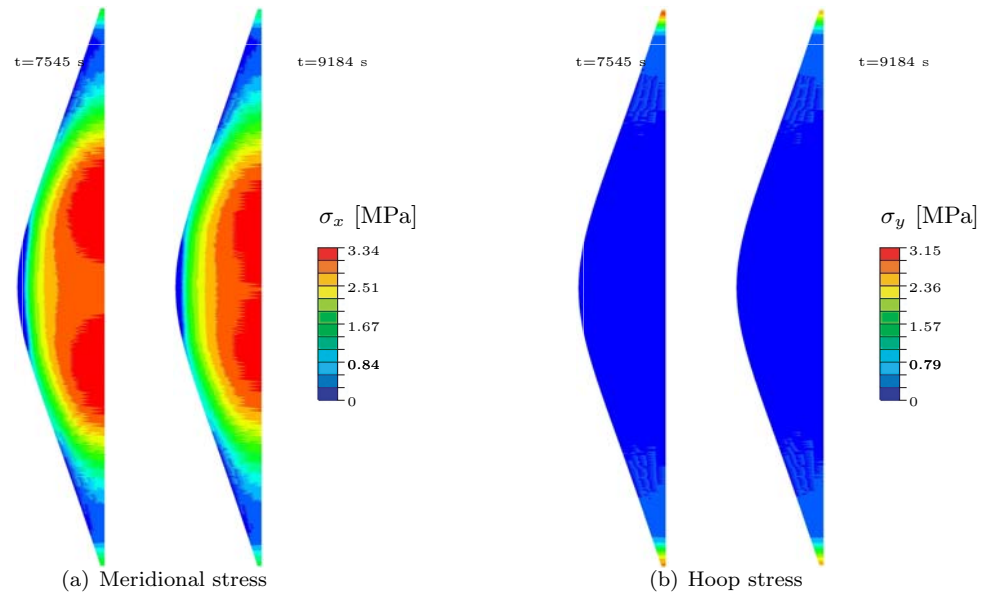


Figure 21: Change of stress distribution during period of constant pressure; before and after 27 min at 120 Pa

The most significant gravity effect was the mass of the components of the balloon; this was included in the simulation but the stress and strain results along the centerline are still almost symmetric, Figure 22. For this reason the strain and stress plots in Figure 24-27 show results only for the top quarter.

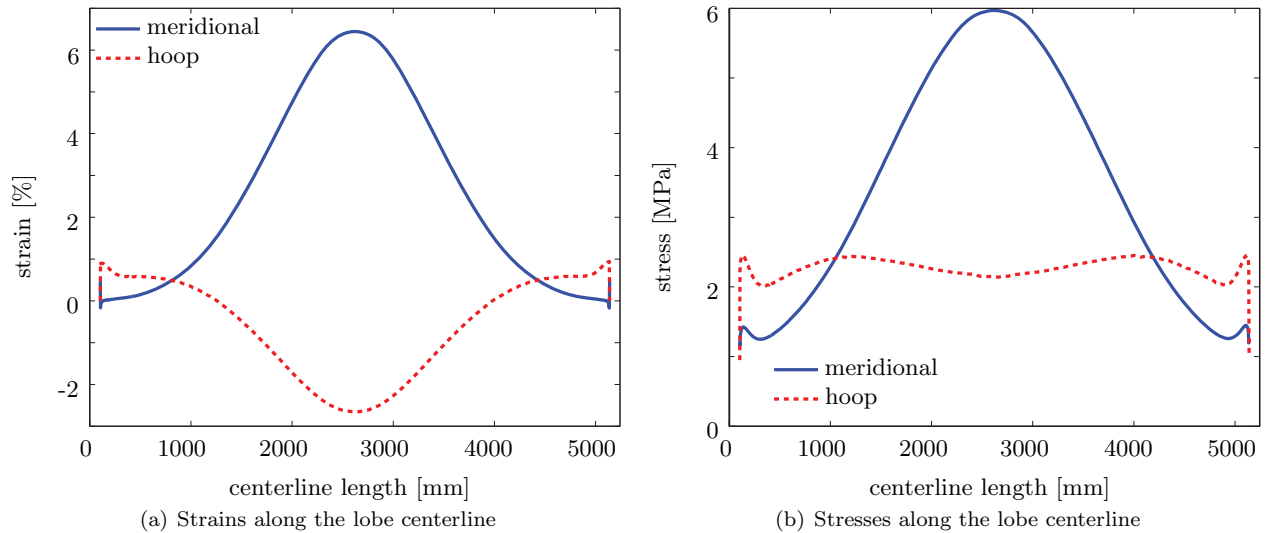


Figure 22: Strains and stresses along the lobe centerline of 4 m balloon; end of 700 Pa pressure hold

In Figures 24 and 25 a continuous representation of the creep strains has been plotted at two different locations along the meridional length; at the equator and at one quarter. In order to capture the variation across the lobe width that has been seen in the snapshots (Figure 18 and 19), for both locations the strains are presented at three positions equally spaced on the half-width of the cutting pattern, as shown in Figure 23.

The overview on the left, Figures 24(a) and 25(a), shows the full time range that was covered including the initial 2 h at 20 Pa. At such low pressures the surface is highly wrinkled and large negative hoop strains appear as a result; the soft overlay elements are effective in allowing the analysis to converge. The detail on the right, Figure 24(b) and 25(b), shows the same strains once the pressure is increased from 20 Pa and the



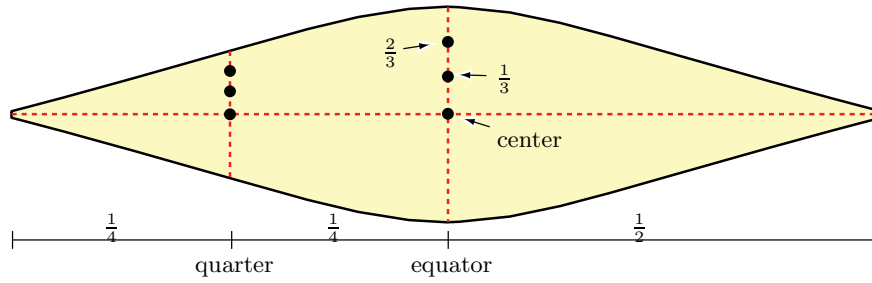


Figure 23: Positions of creep strain output from Abaqus

film becomes less wrinkled.

With increasing pressure, the meridional strains gradually increase to just over 6 percent at the equator, while the center hoop strains remain fairly constant between -2.5 and -3 % at pressures of 120-700 Pa. At one quarter the situation is the other way around: the meridional strains remain fairly constant at 1.7 %, while the hoop strains gradually change from almost -1 % to just above zero.

The stress distribution at the same locations has been plotted in Figure 26. The meridional stress shows both at the equator and at one quarter a characteristic relaxation behavior. The meridional stress variation shows a very steep slope every time the pressure is increased and then a gradual decline as the stress relaxes as the material creeps. In addition there is a 20 % reduction of meridional stress across the lobe width. The hoop stress increases with the applied pressure but otherwise remains constant over time. Also the hoop stress variation across the lobe is small. These observations are valid for both the equator and one quarter locations.

A comparison of results from experiment and numerical analysis, in Figure 27, sheds light on the quality of the finite element model. The bold black lines are the simulation results at the lobe center in the meridional and hoop direction. The thin coloured lines are the experimental mean strains from three lobes as presented in Section 6.6.2. More details on the experimental results can be found in reference 2.

At the equator the creep behavior with respect to the slope of the creep strain is well represented by the model. However, the simulation generally overestimates meridional strains by 0.8-1.5 % in the meridional direction, and underestimates hoop strains by 0.8-1 %. A different situation is observed at one quarter. The meridional creep behavior appears somewhat different: while the experimental creep strains are continuously increasing, the numerical strains remain fairly constant. Generally the strain predictions are about right at one quarter.

Finally the balloon shape measurements are compared to the corresponding finite element model results. The balloon height was defined as the distance between the end-fittings. Generally the overall balloon shape prediction shows little or no time variation at constant pressure. The only changes in height were observed at a pressure of 120 Pa (5.6 mm or 0.22 % increase after 27 min). However, it was not possible to capture such little changes of balloon height in the shape measurements. At pressures of 120-700 Pa there is a constant height difference of about 20 mm between experiment and simulation. At 20 Pa the difference is 170 mm.

A shape comparison, Figure 29, by means of the line half-way between the tendons (centerline) reveals that the model is not just stretched in height, but also the balloon radius appears larger in the simulation. The summation of the line increments between experimental targets and simulation nodes, respectively, shows that the centerline in the simulation is longer, Table 4. The 4 m balloon cutting pattern presented in Section 6.1.2 has a length of 5242.6 mm; 32 mm longer than the centerline length that was measured at 20 Pa (5210.6 mm). Otherwise the shape of the centerline curves agrees well at 120 and 700 Pa.

Table 4: Lobe centerline lengths from apex to base end-fitting center

pressure [Pa]	20	120	700
experiment mean [mm]	5210.6	5252.0	5315.7
simulation [mm]	5254.5	5315.2	5375.1
difference [mm]	42.9	63.3	59.4



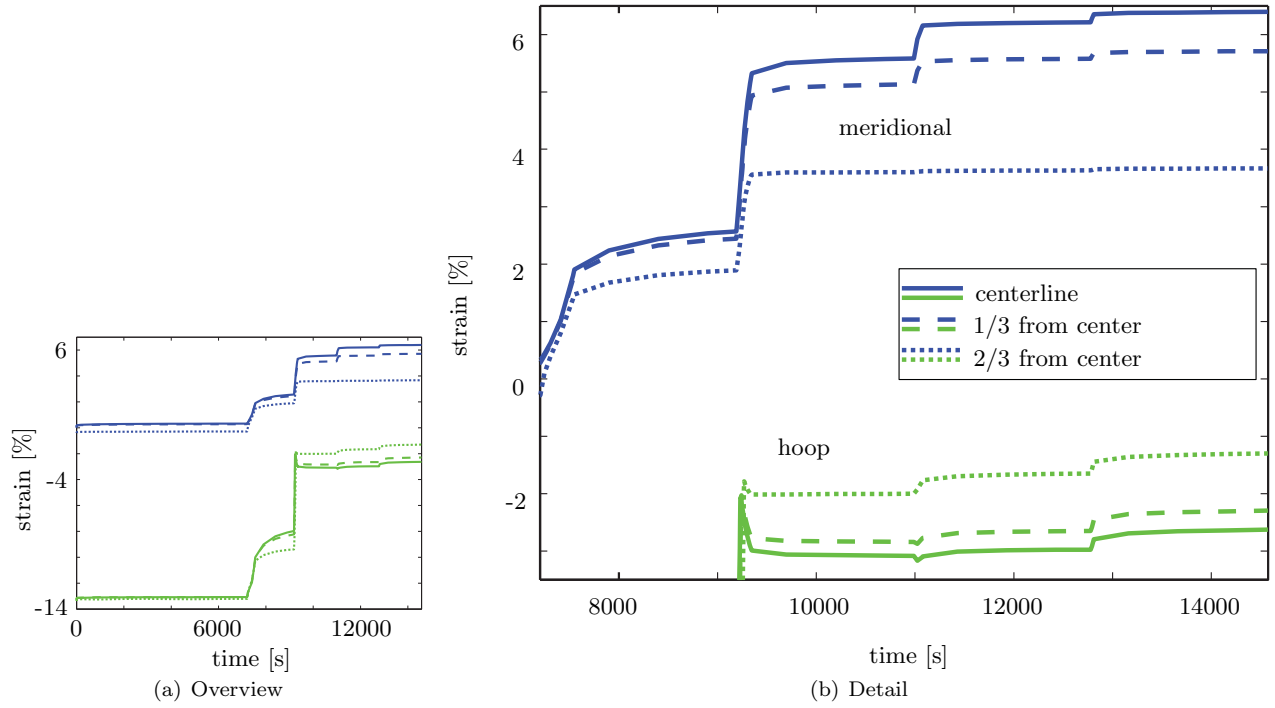


Figure 24: Abaqus strain at the equator

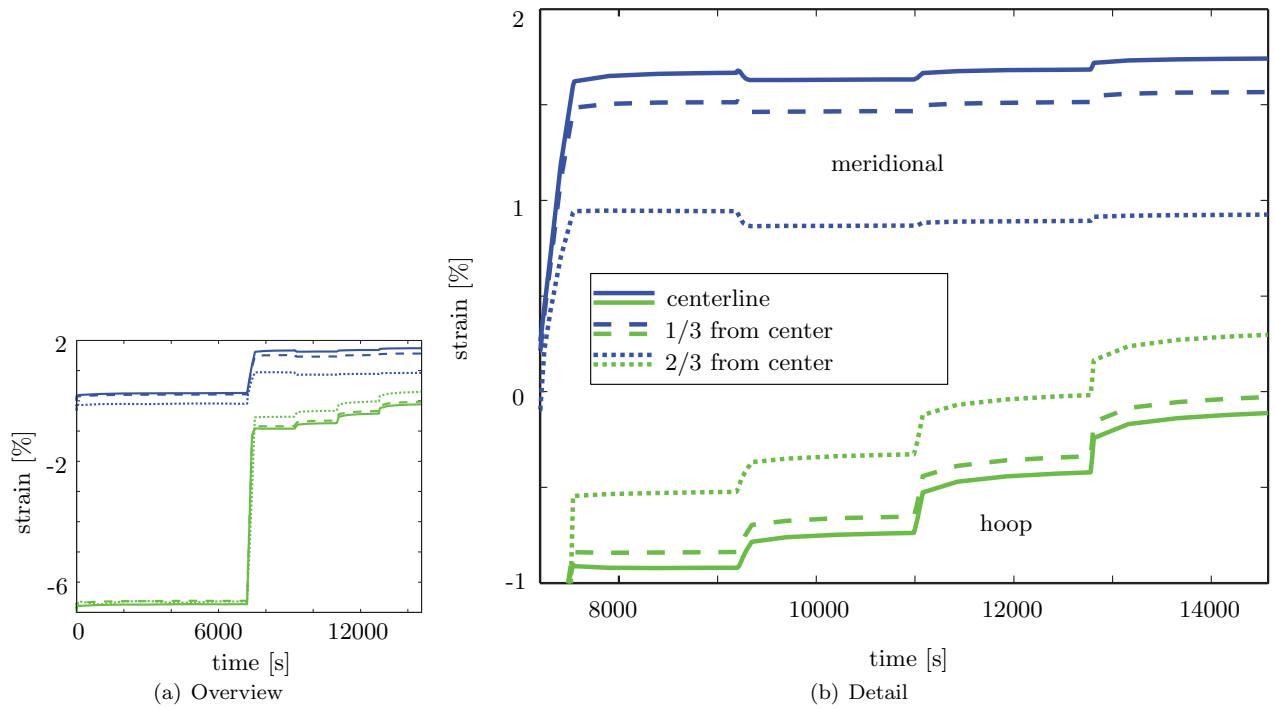
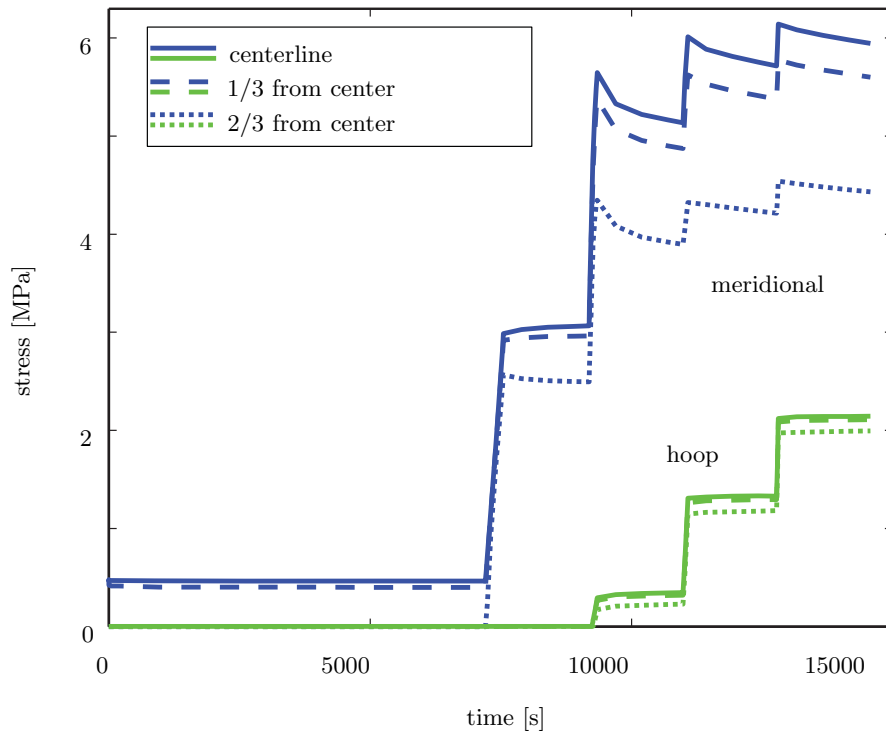
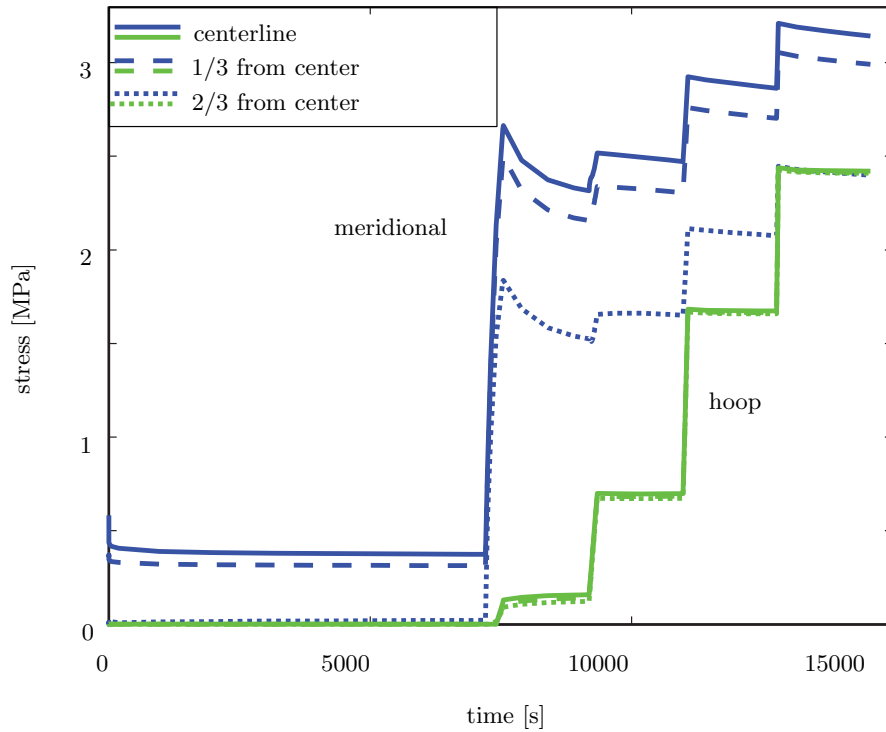


Figure 25: Abaqus strain at one quarter

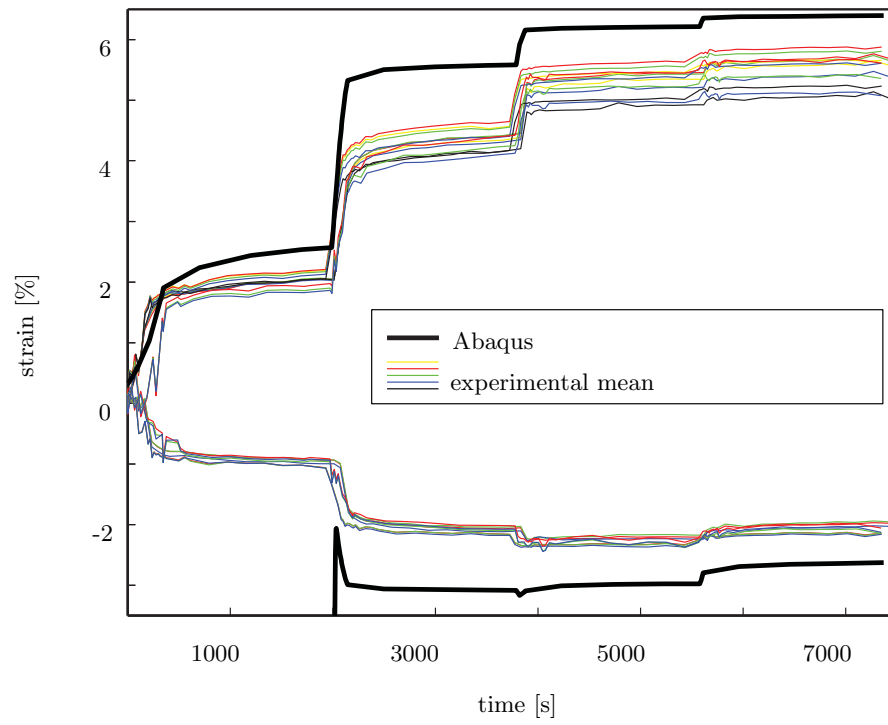


(a) Stress at equator

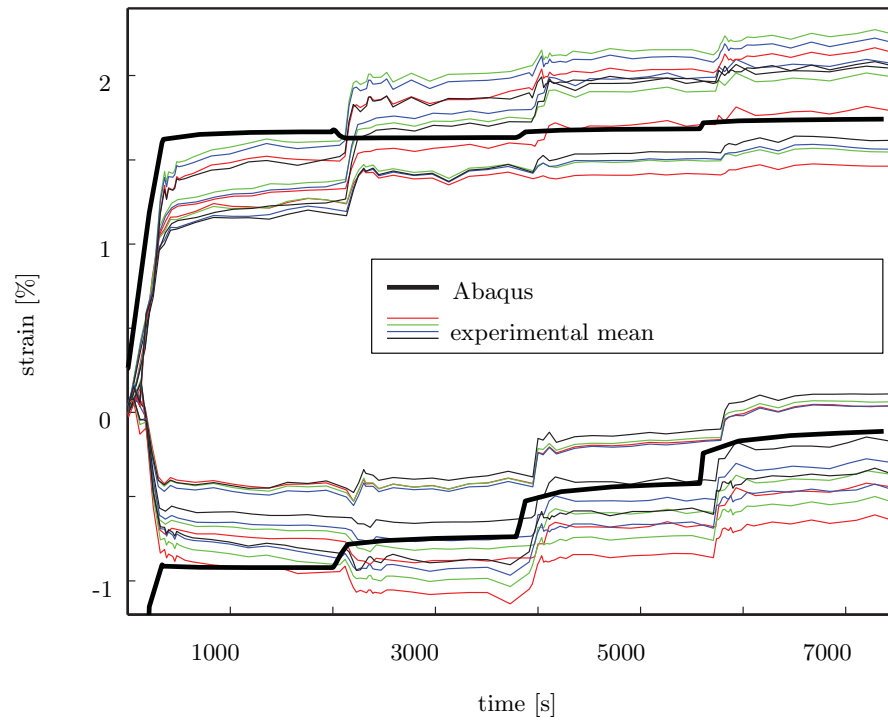


(b) Stress at one quarter

Figure 26: Stresses at  $T = 296$  K



(a) Strain at equator



(b) Strains at one quarter

Figure 27: Comparison of strains

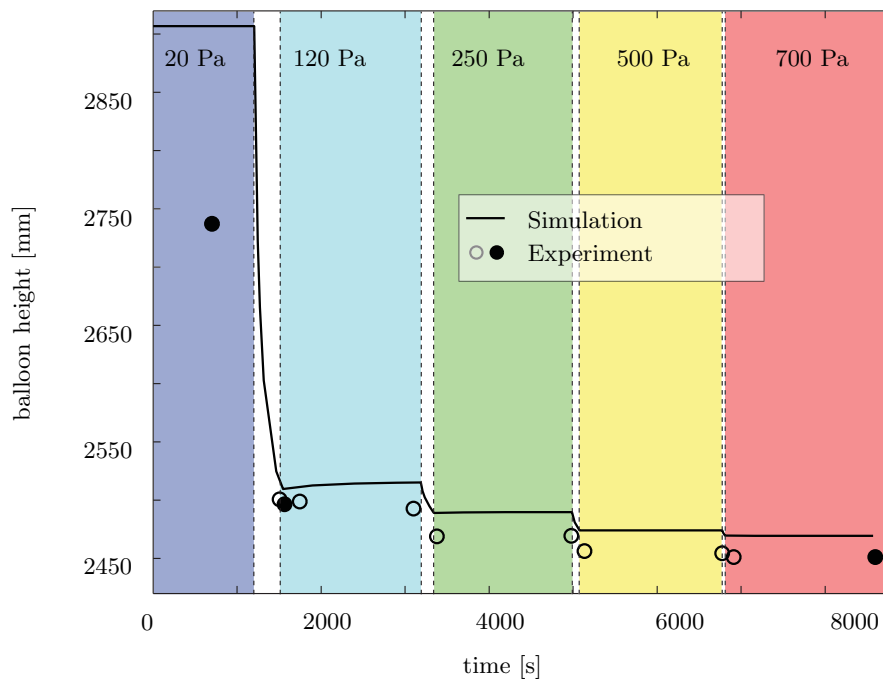


Figure 28: Comparison of end-fitting distance, three full dots correspond to centerlines in Figure 29

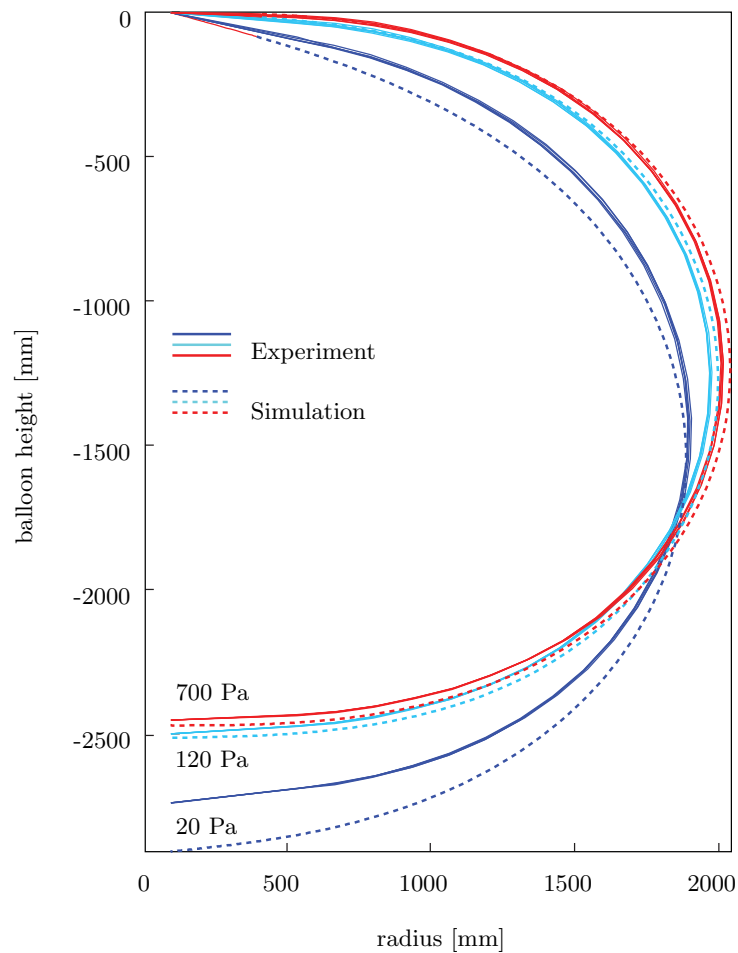


Figure 29: Comparison of meridional shape at three different pressures

## VII. Detailed Model of a Seam

One of the construction details neglected in the finite element model described in Section V is the actual geometry of the seam and tendon attachment between the lobes. The tendon is not attached all the way, but is freed from the seam assembly about 320 mm before it reaches the end-fitting. The tendon end is then attached to a pin at the end-fitting. This tendon attachment has been found to be misaligned from the natural run of the seam by 1-2 pins.

### VII.A. Model Description

Considering the seam detail means that there is no mirror symmetry about the meridional plane through the center of the lobe. Hence, the full lobe width needs to be modeled. To reduce the size of the finite element model, symmetry across the equator is assumed by neglecting gravity effects. In addition, a pseudo-elastic material model was adopted, as a full viscoelastic analysis would take too long. The moduli  $E_1$  and  $E_2$  in the two material directions were taken as 167 MPa and 214 MPa, respectively, based on a the assumption of  $T=283$  K,  $\sigma_1=4.5$  MPa,  $\sigma_2=5.0$  MPa,  $t=400$  s.

For the numerical model the cutting pattern was kept unchanged while the seam was cut in two parts, which were modeled as attached to the left and right edges of the gore model, Figure 30(b). Both seam parts were modeled as single sheet membranes with their thickness corresponding to the total thickness of the film layers included in the actual seam. One seam part contained the tendon. The displacement of the tendon end-fitting attachment by 18.2 mm (distance between 2 pins for tendon attachment at the end-fitting) results in a kink in the tendon with angle  $\alpha$ , Figure 31.

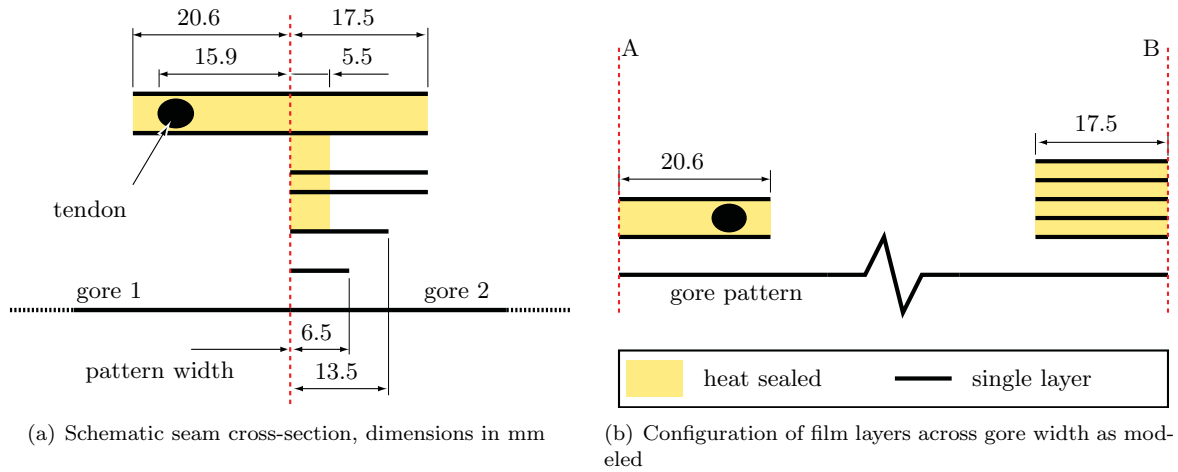


Figure 30: Seam schematic with various film layers, reality vs. model

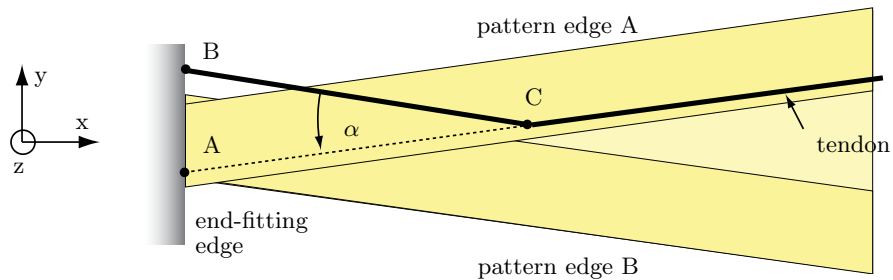


Figure 31: Schematic of end-fitting area with two seam strips and tendon; end-fitting attachment of tendon displaced from A to B

### VII.A.1. Mesh and Elements

For the finite element model the same element types were used as in Section V; three-node triangular membrane elements (M3D3) and two-node truss elements (T3D2). The mesh consisted of a total of 14678 nodes and 27110 membrane elements; 20579 elements for the pattern, 1338 elements for the seam attached to edge B, 5193 elements for the seam containing the tendon. The mesh density for the gore was highest along the tendon (minimum element side length 2 mm) and coarsest at the equator center (maximum element side length 30 mm). In the two seam strips the element side lengths range between 3 and 8 mm.

A set of overlaid membrane elements was used to improve convergence in heavily wrinkled areas (see Section 7.1.3). The overlaid membranes had a stiffness of  $E=1$  MPa and prestresses of  $\sigma_x=0.05$  MPa and  $\sigma_y=0.18$  MPa ( $\sigma_y=0.1$  and  $0.15$  MPa for the two seam strips).

### VII.A.2. Boundary Constraints

Boundary constraints along the edges labeled as A and B in Figure 30(b) were enforced using `*equation` in a local cylindrical coordinate system. The nodes along the edges were constrained to have the same vertical, radial and circumferential displacement while maintaining a  $7.5^\circ$  lobe opening angle. Therefore the nodes along the two pattern edges (A and B) and the dummy nodes were transformed into a local cylindrical coordinate system using the command `*transform, type=C` such that the balloon axis became the  $z$ -axis of the cylindrical system. The `*equation` constraint to attach one seam strip to edge A (see Figure 30(b)) was then written as

$$\begin{aligned}\Delta x_{seam} - \Delta x_{edgeA} &= 0 \\ \Delta y_{seam} - \Delta y_{edgeA} &= 0 \\ \Delta z_{seam} - \Delta x_{edgeA} &= 0\end{aligned}\tag{29}$$

and similarly for the other seam strip and edge B. In addition a set of equations was written to define the movement of each individual node on edge A as equal to the movement of a corresponding node on edge B:

$$\begin{aligned}\Delta x_{edgeA} - \Delta x_{edgeB} &= 0 \\ \Delta y_{edgeA} - \Delta y_{edgeB} - \Delta y_{dummies} &= 0 \\ \Delta z_{edgeA} - \Delta x_{edgeB} &= 0\end{aligned}\tag{30}$$

### VII.A.3. Contact Constraints

The contact constraint between the seam and the gore was modeled as `tied contact`, where contact is maintained between two surfaces once it has been established at the beginning of an analysis. `Tied contact` constrains each of the nodes on the slave surface to have the same displacement as the point on the master surface that it contacts.

The membrane elements of the two seam strips defined two element-based master surfaces. Two corresponding node-based slave surfaces were defined on the gore including 8009 nodes within a 25 mm wide band along the cutting pattern edge. Tied contact was defined in the model definition with the command `*contact pair, tied, adjust=1.0`. Contact between the symmetry plane and the lobe surface was not implemented, since a combination of tied contact and self contact is not permitted in Abaqus. As a consequence self-contact of the membrane around the tendon was observed at a pressure below 330 Pa.

Two limitations of the tied contact model were observed: firstly, no contact formulation was enforced between the free tendon and the membrane, since the free tendon section between end-fitting and seam-entry was modeled with one truss element that cannot be used to define a contact surface. Hence, where the tendon was detached the membrane could bulge freely when the pressure was applied. Secondly, the tied contact prevents the buckling of the seam and consequently the seam remains in contact even where the tendon is entering the seam. Figure 32 shows the observed buckling and slipping of the seam in the physical structure.

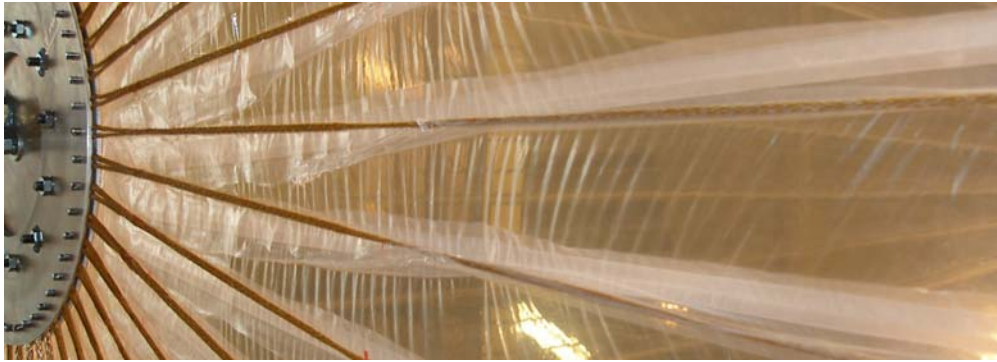


Figure 32: Tendon enters the seam; buckling and slipping of seam observed

## VII.B. Results

The stress and strain distribution in the gore at two different pressures, 300 and 1000 Pa, has been plotted in the top half of Figures 33 to 34. For comparison the simulation of the balloon as been rerun using the standard finite element model from Section V with the same pseudo-elastic properties ( $E_1=167$  MPa,  $E_2=214$  MPa). The corresponding strain and stress distribution have been plotted in the lower half. Note that the high stresses are due to the relatively stiff pseudo-elastic properties. Their choice was arbitrary and not bound to a particular temperature, time or state of stress.

The results from the detailed model are slightly un-symmetric across the gore width. The peaks of the strains in both directions and the meridional stress have shifted to the right, only the hoop stresses appear symmetric. Both meridional and hoop stresses are very low where the gore is supported by the extra layers of film of the seam. These observation are valid at both pressure levels.

The lack of symmetry across the gore width becomes apparent when one takes a cross-section of the lobe at the equator, Figure 35. An indentation forms along the tendon (on the left) and the two seam strips are part of the lobed shape. At a pressure of 300 Pa the lobed shape shows a valley on the right due to the additional structural stiffness along the seam, Figure 35(a). This effect decreases with increasing pressure. Since self-contact in the tendon area was not prevented, a penetration of the membrane surface is observed for pressures less than 330 Pa, Figure 35(a). This is in contrast to the experimental observations, where the up to five times thicker seam has some bending stiffness and resists small negative hoop stresses. Consequently in the physical structure at low pressures the seam does not fold around the tendon, but takes a rather flat shape.

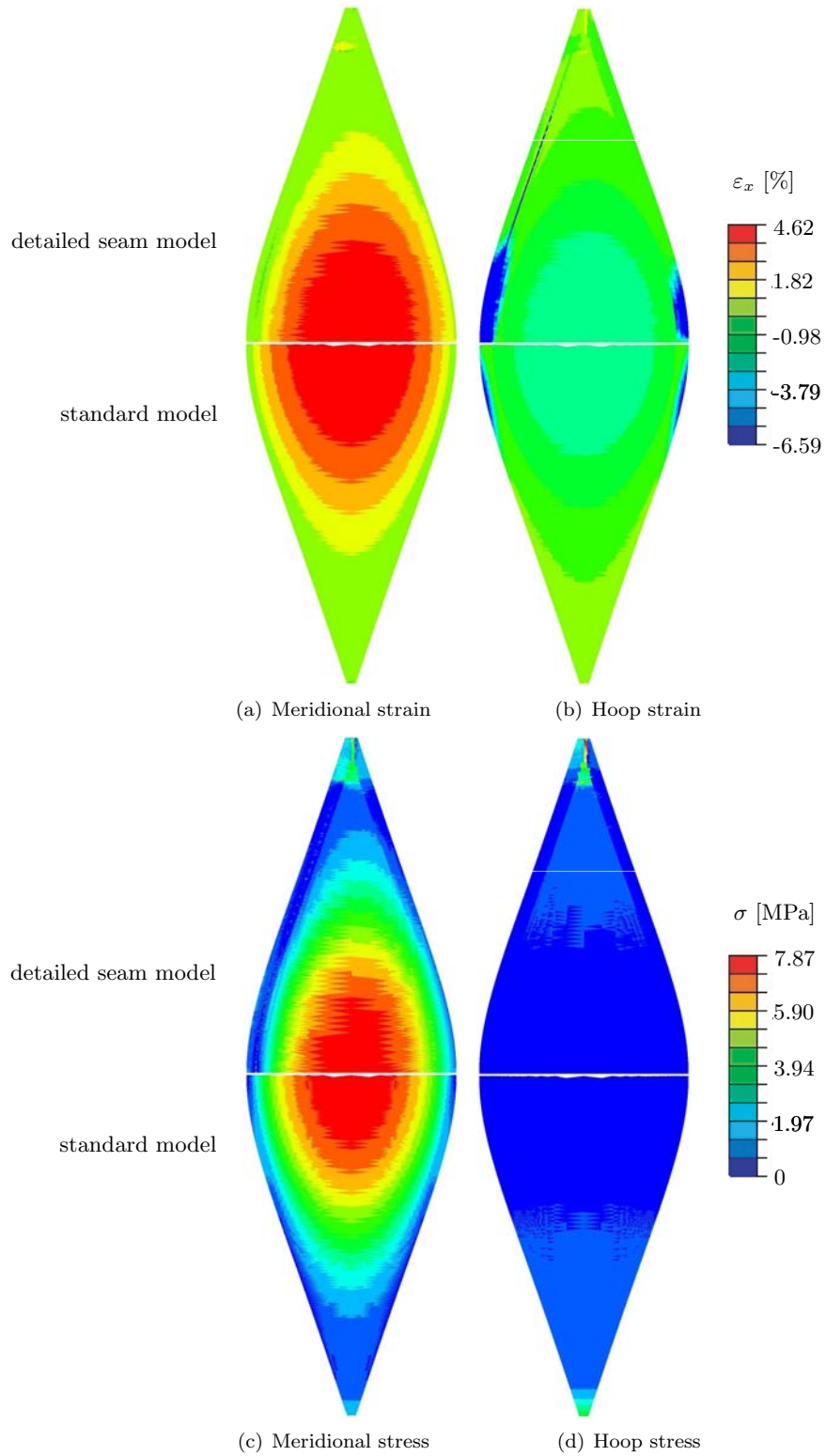


Figure 33: Strain and stress distribution at a pressure of 300 Pa; comparison of detailed and simplified seam model



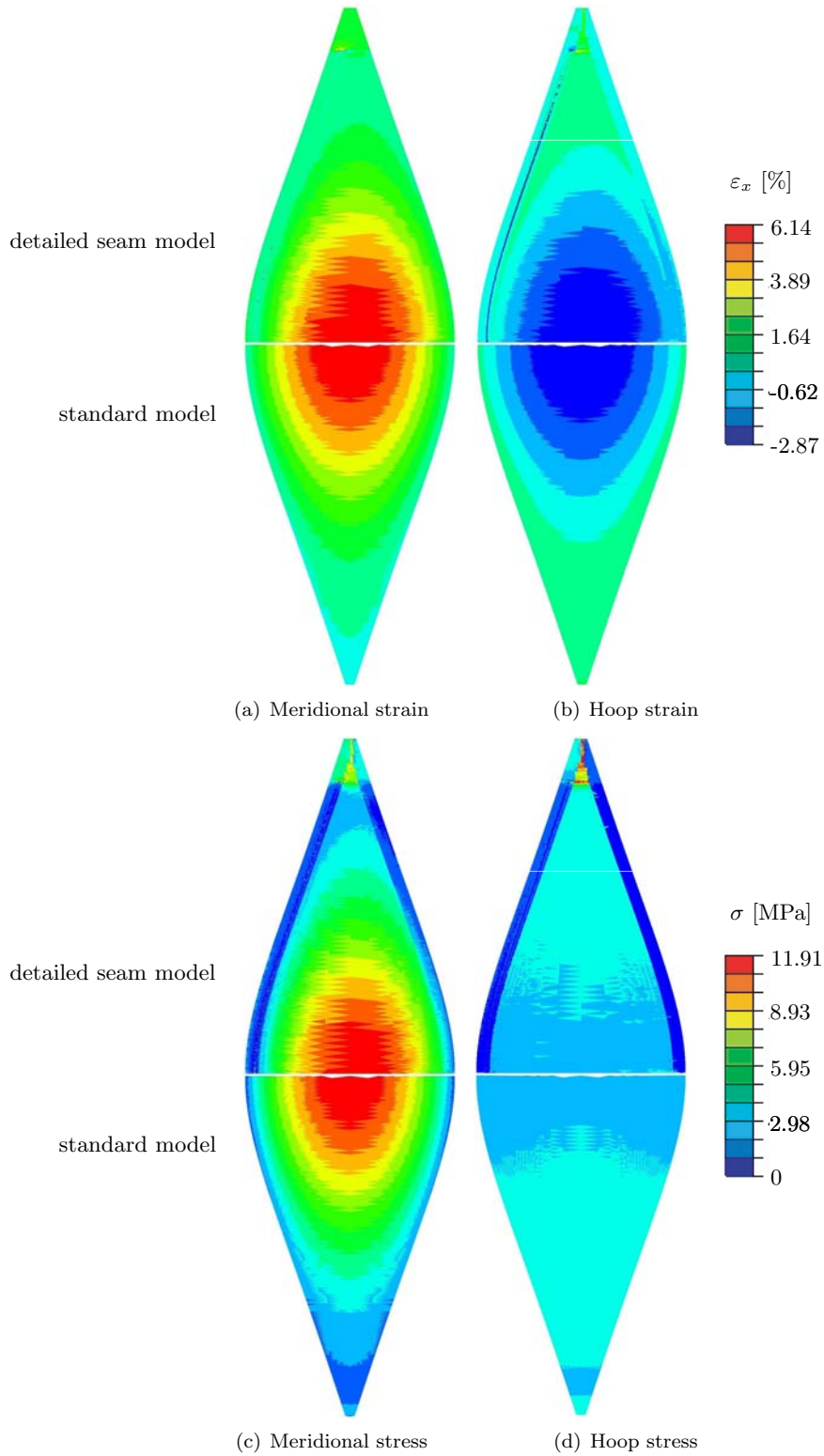


Figure 34: Strain and stress distribution at a pressure of 1000 Pa; comparison of detailed and simplified seam model

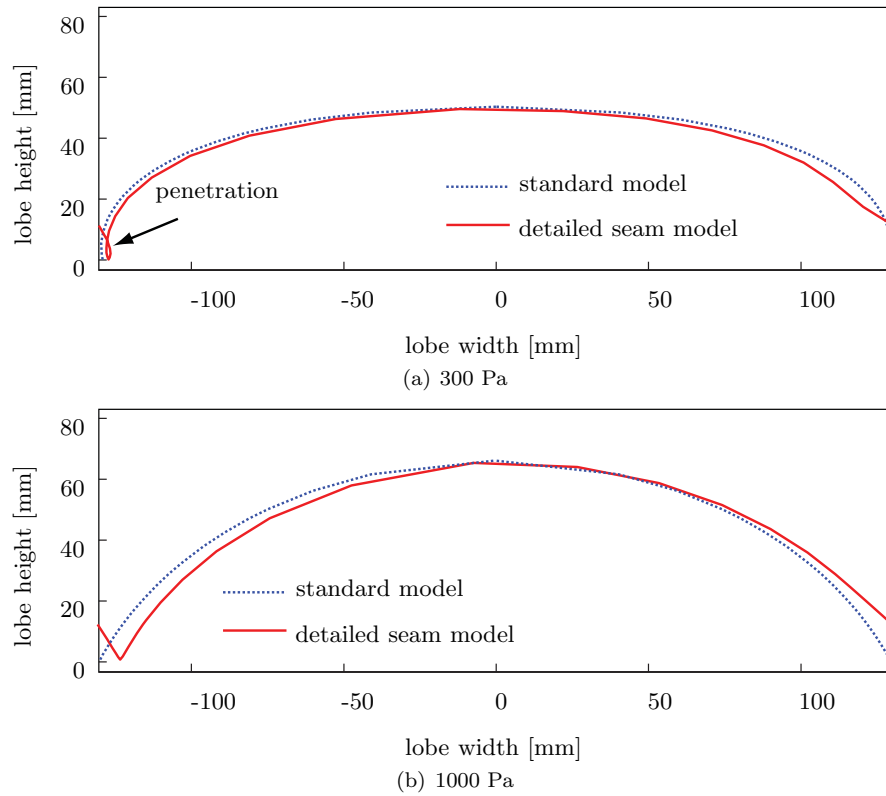


Figure 35: Comparison of equator cross-sections of the lobe; simplified vs. detailed seam model

### VII.C. Swirl of End-Fittings

The misalignment of the tendon attachment by 1 or 2 pins during the production of the balloon causes a kink in the natural run of the tendon, referred to as swirl. Figure 36(a) shows the balloon at a pressure of less than 5 Pa. The swirl is visible where the tendon enters the seam about 320 mm from the end-fitting. In Figure 36(b) the balloon was pressurized to 700 Pa and the swirl almost completely disappeared. Only a few tendons were left with a slight swirl. Note how the initially straight seam is deformed as the tendon straightens at a higher pressure.



(a) Swirl of tendons at lower pressures (10 Pa)



(b) Straight tendons at higher pressure (700 Pa)

Figure 36: Tendon swirl in the end-fitting area at low and high pressure

This phenomenon was replicated in the finite-element model. The lobe section in Figure 37(a) shows the onset of the simulation with the tendon highlighted in red. The lobe section in Figure 37(b) was obtained at 1000 Pa and shows the tendon almost straightened.

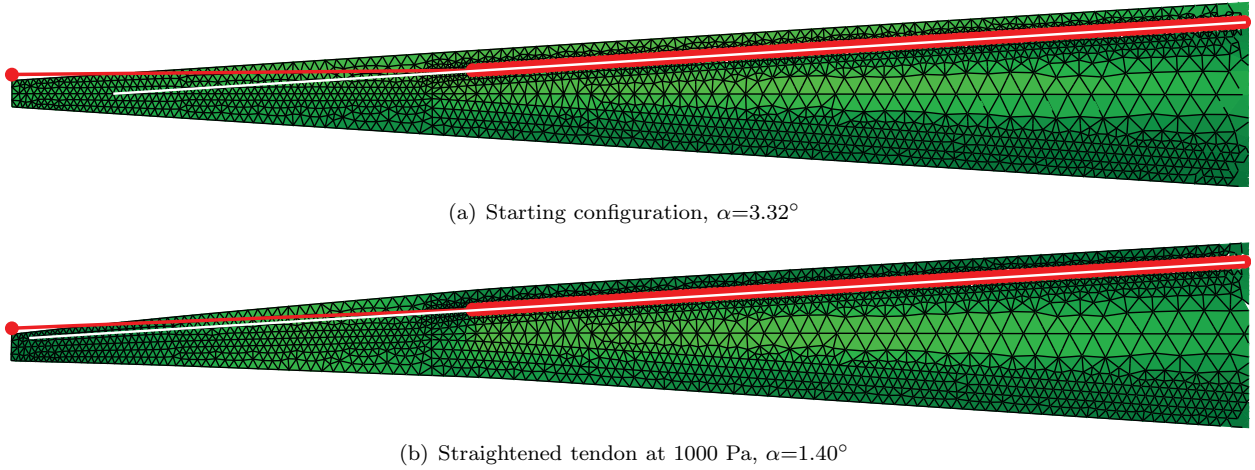


Figure 37: Comparison of starting configuration of tendon versus straightened tendon

The initial swirl gradually disappears as the stiff tendons take proportionally higher stresses at increasing pressure. This is accompanied by a rotation of the end-fitting and a decrease of the kink angle  $\alpha$  (see Figure 31). In Figure 38  $\alpha$  was plotted with increasing pressure. The starting configuration of  $\alpha = 3.32^\circ$  has been assigned to zero pressure. The simulation considered pressures ranging from 300 to 1000 Pa. The dotted line has been interpolated.

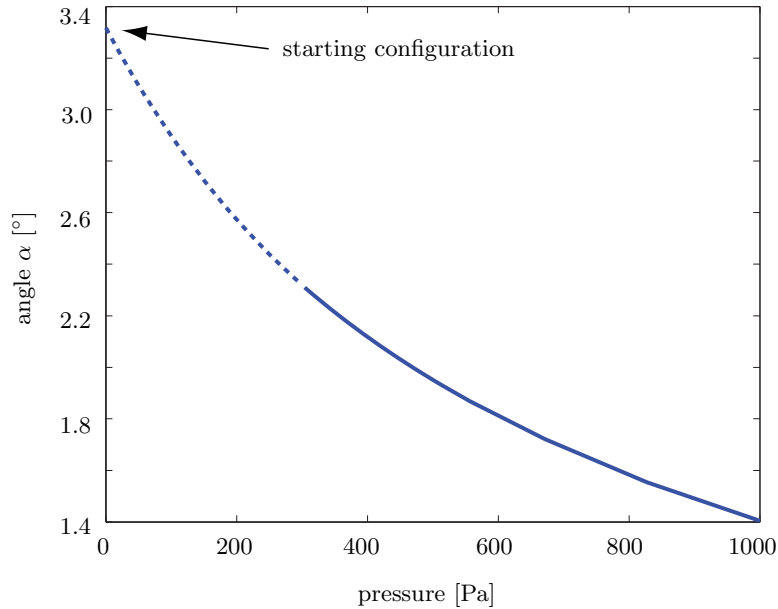


Figure 38: Decrease of angle  $\alpha$  with increasing pressure

## VIII. Discussion and Conclusion

This research was motivated by the need for a reliable prediction of stresses and strains that occur during the flight of super-pressure balloons. Viscoelasticity plays a major role in the stress and strain distribution in balloon structures. The film creeps as time passes, causing the stresses to redistribute. While initially

relatively high stresses can be caused by the pressurization of the structure, these stresses relax as time passes and a more even stress distribution is reached eventually. Although an initial version of the material model had been published, nonlinear viscoelastic simulations of super-pressure balloons were missing. This was mainly due to the lack of a suitable numerical implementation of the material model. At the same time experimental data from balloon structures was limited and time-dependence was not included. There was only little knowledge about the time-dependent strain and stress distribution in an actual balloon structure and hence it was not possible to validate the material model. As a consequence the material model, the numerical simulations and the experimental data were somewhat disconnected. The present work has closed the gap between theory and experimental observation.

The integral formulation of the nonlinear viscoelastic material model proposed by Rand has been rewritten in incremental form and implemented in Abaqus. In addition a formulation for wrinkling in orthotropic membranes has been developed and implemented. The two separate implementations of wrinkling and viscoelasticity have been combined in a single user-defined subroutine in Abaqus. In heavily wrinkled cases an overlay with a very soft and pre-tensioned membrane was adopted to provide some residual stiffness at all times. Models with only some wrinkled areas worked well without this trick.

For the measurement of creep strains in actual balloon structures a contact-free experimental method based on photogrammetry has been developed. Experiments have been done on a 4 m balloon. Measurements included creep strains under biaxial and uniaxial load cases. Experiments on balloon structures focused on the measurement of local creep strains and the overall shape of a balloon.

The newly developed numerical tools were applied to a 4 m diameter balloon model with a distinctly lobed shape. At a pressure of 700 Pa the balloon showed a maximum stress of 6.0 MPa in the meridional direction (2.5 MPa hoop stress) and meridional strains of up to 6.4% (-2.7% hoop strain).

The viscoelastic behavior was accurately predicted at the equator although strains were generally over-estimated. However, at a quarter of meridional length, where the stresses are more balanced, the predicted creep behavior was less accurate. Generally a better agreement was found where stresses were less balanced. Excellent results were obtained under uniaxial stress, while biaxial stress states were found very sensitive to small structural variations. These discrepancies indicate that further refinements are still needed in the viscoelastic material model of SF420.

The effects from additional detail in the model were analyzed by including the seam-tendon assembly and tendon-end-fitting attachment. For simplicity this simulation was done only using pseudo-elastic properties instead of a full viscoelastic model. The resulting lobe shape had the meridional indentation along the tendons and a deformation of the lobed shape becomes visible at pressures up to about 500 Pa due to the higher stiffness of the seam. In addition the phenomenon of a swirl in the end-fitting area was replicated in the simulation. The initial kink angle in the tendon reduced from  $3.4^\circ$  to  $1.4^\circ$  when a pressure of 1000 Pa was applied. During their shape-finding the comparably stiff tendons straighten and depending on the differential pressure in the balloon this leads to a rotation of the end-fitting.

## Acknowledgments

We thank the NASA Superpressure Balloon Team team for their contribution to this research. We are grateful to Henry Cathey and Leyland Young (NMSU Physical Science Laboratory) for providing test data and to Debora Fairbrother and Rodger Farley (NASA), Jim Rand (Winzen Engineering) and David Wakefield (Tensys) for helping us through numerous discussions. This research was supported by the NASA Balloon Program Office (contract monitor Danny Ball) headed by David Pierce. Special thanks go to Loren Seely (Aerostar) for providing the balloon structure for this research and to Mike Smith (Aerostar) for his advice.

## References

- <sup>1</sup>CATHEY, H.M., STERLING, J., YOUNG, L.G., GARDE, G.J., PIERCE, D. ULDB 48 Gore Flat Facet Balloon Strain Arrest Test Report. Report, Physical Science Laboratory and NASA Code 541, 2007.
- <sup>2</sup>GERNGROSS, T. Viscoelastic behavior in Stratospheric Balloon Structures. PhD thesis (submitted), University of Cambridge, Department of Engineering, 2009.
- <sup>3</sup>GERNGROSS, T., XU, Y., AND PELLEGRINO, S. Viscoelastic behavior of pumpkin balloons. *Advances in Space Research*, **42**, 10, 1683-1690, 2007. doi:10.1016/j.asr.2007.03.093.

- <sup>4</sup>GERNGROSS, T., AND PELLEGRINO, S. Modelling of Anisotropic Viscoelastic behavior in Super-Pressure Balloons. 48th AIAA/ASME/ASCE/AHS/ASC Structures, Structural Dynamics and Materials Conference, AIAA-2007-1808.
- <sup>5</sup>GERNGROSS, T., AND PELLEGRINO, S. Implementation and Validation of Schapery-Rand Anisotropic Viscoelasticity Model for Super-Pressure Balloons. AIAA Balloon Systems Conference, 21-24 May, 2007, Williamsburg, VA, AIAA-2007-1808.
- <sup>6</sup>HAIJ-ALI, R.M., AND MULIANA, A.H. Numerical finite element formulation of the schapery nonlinear viscoelastic material model. *International Journal for Numerical Methods in Engineering*, **59**, 25-45, 2004.
- <sup>7</sup>KANG, S., AND IM, S. Finite element analysis of wrinkling membranes. *Journal of Applied Mechanics*, **64**, 263-269, 1997.
- <sup>8</sup>MCCRUM, N.G., BUCKLEY, C.P., AND BUCKNALL, C.B. *Principles of Polymer Engineering*, 2nd edition ed. Oxford Science Publications, Oxford, 2003.
- <sup>9</sup>MILLER, R.K., AND HEDGEPEETH, J.M.. An algorithm for finite element analysis of partly wrinkled membranes. *AIAA Journal* 1982, **20**, 12, 1761-1763, 1982.
- <sup>10</sup>MILLER, R.K., HEDGEPEETH, J.M., WEINGARTEN, V.I., DAS, P., KAHYAI, S.. Finite element analysis of partly wrinkled membranes. *Computers and Structures*, **20**, 1-3, 631-639, 1985.
- <sup>11</sup>RAND, J.L. An Improved Constitutive Equation For SF420 Part 1: The Master Curve. Internal Report, Winzen Engineering Inc, 2008.
- <sup>12</sup>RAND, J.L. An Improved Constitutive Equation For SF420 Part 2: The Biaxial behavior. Internal Report, Winzen Engineering Inc, 2008.
- <sup>13</sup>RAND, J.L., GRANT, D.A., AND STRGANAC, T. The nonlinear biaxial characterization of balloon film. 34th AIAA Aerospace Sciences Meeting and Exhibit, AIAA-96-0574, 1996.
- <sup>14</sup>RAND, J.L., AND STERLING, W.J. A constitutive equation for stratospheric balloon materials. *Advances in Space Research*, **37**, 11, 2087-2091, 2006.
- <sup>15</sup>SCHAPERLY, R.A. On the characterization of nonlinear viscoelastic materials. *Polymer Engineering and Science*, **9**, 4, 1969.
- <sup>16</sup>SCHAPERLY, R.A. Nonlinear viscoelastic and viscoplastic constitutive equations based on themodynamics. *Mechanics of Time-Dependent Materials*, **1**, 209-240, 1997.
- <sup>17</sup>SMITH, M.S., AND CATHEY, H.M. ULDB Phase 7-a, Four Meter Pumpkin Model No.1, Test Report. unpublished internal report, Raven Industries, Sulphur Springs, TX, March 2004.
- <sup>18</sup>WARD, I.M. *Mechanical Properties of Solid Polymers*, 2nd edition. John Wiley & Sons, 1985.